DR. PABLO SUAREZ-GONZALEZ (Orcid ID : 0000-0002-2370-5017)
DR. M. ISABEL BENITO (Orcid ID : 0000-0002-8711-0864)
DR. CONCHA ARENAS (Orcid ID : 0000-0002-4212-0524)

Article type : Themed Issue Paper

Corresponding author mail id: pablosuarez@ucm.es

Columnar microbialites of the upper Miocene of Mallorca (Spain): A new morphogenetic model based on concurrent accretion and bioturbation – uncommon or overlooked?

Pablo Suarez-Gonzalez[1], M. Isabel Benito[1, 2], Concha Arenas[3], Luis Pomar[4]

[1]Dpto. de Geodinámica, Estratigrafía y Paleontología, Facultad de Ciencias Geológicas. Universidad Complutense de Madrid. c/ José Antonio Novais, 12, 28040 Madrid, Spain.
[2]Instituto de Geociencias (IGEO). CSIC-UCM. c/ José Antonio Novais, 12, 28040 Madrid, Spain.
[3]Dpto. de Ciencias de la Tierra, Facultad de Ciencias, Instituto Universitario de Investigación en Ciencias Ambientales de Aragón (IUCA) and Geotransfer Group, Universidad de Zaragoza, c/ Pedro Cerbuna, 12, 50009, Zaragoza, Spain.
[4]Cátedra Guillem Colom, Universitat de les Illes Balears, ctra. Valldemossa, km 7.5, 07122 Palma de Mallorca, Spain.

Running title: Bioturbation-influenced columnar microbialites

Associate Editor – Guillem Mateu-Vicens

ABSTRACT

Bioturbation has long been considered an antagonist of microbialite development and preservation, because metazoan grazing and burrowing destroy benthic microbial communities. However, metazoan bioturbation, in conjunction with microbial accretion, may have had a

This article has been accepted for publication and undergone full peer review but has not been through the copyediting, typesetting, pagination and proofreading process, which may lead to differences between this version and the Version of Record. Please cite this article as doi: 10.1111/sed.12850

significant role in the morphogenesis of some columnar microbialites, as suggested by the case study presented and by some Phanerozoic and Upper Proterozoic analogues discussed here. Late Miocene in age, the studied microbial biostrome developed in a western Mediterranean restricted shallow-water platform dominated by grainy sediments and with a notable influence of bioturbation. This study is focused on the complex accretionary history of the columnar microbialite biostrome and on its striking dark grey colour, which is attributed to Mn-oxyhydroxides precipitated during meteoric diagenesis linked to subaerial exposure. The characteristic columnar structure of the microbialite biostrome has features consistent with an accretionary origin of the columns, but also has features suggesting metazoan disruption. Therefore, a new morphogenetic model for columnar microbialites is presented, highlighting the concomitant roles of microbial accretion, bioturbation and grainy sediment infill of the intercolumn space. Whether this model is an exception or a rule, should be tested on other examples of Phanerozoic and Upper Proterozoic columnar microbialites. Nevertheless, this model is a step forward in understanding the complex microbe–metazoan interactions as constructive coexistence rather than just as destructive competition.

Keywords

Bioturbation; boring; burrowing; diagenesis; grazing; manganese; microbialite morphogenesis; stromatolite biostrome.

INTRODUCTION

Microbialites are organosedimentary structures formed through the interaction of benthic microbial communities and their environmental conditions (e.g. Golubic, 1976; Burne & Moore, 1987; Riding, 2011). This relatively simple definition hides a vast complexity developed over 3500 million years, since microbialites are one of the earliest signs of life recorded in Earth history, and are still significantly widespread (Grotzinger & Knoll, 1999; Reitner *et al.*, 2011; Chagas *et al.*, 2016; Schirrmeister *et al.*, 2016). This complexity can be seen in the diversity of sedimentary environments where microbialites occur, in their abundance and diversity of sizes, shapes and internal structures and in their variability through time (e.g. Hofmann, 1969; Awramik, 1971; Walter, 1972; 1976; Monty, 1973; 1976; Hoffman, 1976a; Awramik & Sprinkle, 1999; Grotzinger & Knoll, 1999; Raaben, 2006; Riding, 2006; 2011; Grey & Awramik, 2020). For that reason, the study of microbialite morphogenesis (i.e. the biotic and abiotic processes underlying microbialite morphology at different scales) has been crucial since the early stages of microbialite studies (e.g. Hoffman, 1976b; Serebryakov, 1976; Walter *et al.*, 1976; Semikhatov *et al.*, 1979; Wright & Mayall, 1981; Vanyo & Awramik 1985; Bertrand-Sarfati *et al.*, 1994; Grotzinger & Rothman, 1996; Grotzinger & Knoll, 1999). However, the recent advances and discussions in that field (e.g. Andres & Reid, 2006; Bosak *et al.*, 2013; Jahnert & Collins, 2013; Ibarra *et al.*, 2014; Vennin *et al.*, 2015; Hickman-Lewis *et al.*, 2019; Martín-Bello *et al.*, 2019; Bourillot *et al.*, 2020) are evidence that the complex combination of microbial and environmental factors that shape microbialites are not fully understood yet.

A particular case of widely-studied microbialite morphology is that of columnar stromatolites with centimetric subcylindrical columns, characteristic of the Proterozoic, when they reached remarkable diversity of sizes and forms (e.g. Awramik, 1971; Walter, 1972; Bertrand-Sarfati, 1972; Awramik & Sprinkle, 1999; Grotzinger & Knoll, 1999; Bosak *et al.*, 2013; Grey & Awramik, 2020). Similar growth forms, however, are much rarer during Phanerozoic times, with only scarce and smaller examples (e.g. Monty, 1973; Andres & Reid, 2006; Bosak *et al.*, 2013; Martín-Bello *et al.*, 2019; see further references in Walter, 1972). Given the archetypical nature of columnar microbialites during the Proterozoic and its Phanerozoic decline, their morphogenesis has received special attention, either through mathematical models (e.g. Grotzinger & Knoll, 1999; Batchelor *et al.*, 2003; Dupraz *et al.*, 2006; Bosak *et al.*, 2013, and references therein), or through the comparative analyses of modern and fossil examples (e.g. Semikhatov *et al.*, 1979; Grotzinger

& Knoll, 1999; Andres & Reid, 2006; Bosak *et al.*, 2013; Hickman-Lewis *et al.*, 2019; Martín-Bello *et al.*, 2019). Virtually all of these examples and models emphasise the origin of microbialite columns as accretionary products of benthic microbial communities interacting with the environment, but only very few examples have highlighted syn-depositional or post-depositional metazoan disruption (i.e. bioturbation) in the morphogenesis of columnar microbialites (Wright & Mayall, 1981; Cao, 1988; Druschke *et al.*, 2009).

This contribution presents the first description of upper Miocene, shallow marine, columnar microbialites that prompt discussion about the potential role of bioturbation processes in the genesis of macroscopic columnar morphology. Bioturbation has traditionally been considered antagonistic to microbialite accretion since the recognition that metazoan grazers and burrowers preyed on benthic microbial communities (e.g. Garrett, 1970; Awramik, 1971; Walter & Heys, 1985). Later, however, it has been shown that other factors besides metazoan disruption were involved in the Proterozoic demise and Phanerozoic variable abundance of microbialites (e.g. Grotzinger, 1990; Riding, 2006; 2011). Therefore, the Miocene columnar examples presented here not only provide a new model for the morphogenesis of microbialite columns, at least in the Phanerozoic, but also widen current understanding of the relationships between microbial accretion and metazoan disruption, offering promising hypotheses for future inquiries into the controls of microbialite morphologies.

GEOLOGICAL SETTING

The studied microbialites crop out in a road cut between Kilometre 1 and 2 of the Ma-6110 road to 'Cap de Ses Salines', at the southernmost part of the island of Mallorca, western Mediterranean (Fig. 1). It is an isolated road cut, surrounded by an extensive flat area without any other significant rock outcrops nearby. Stratigraphically, it belongs to the Santanyí Limestone, which is time-equivalent to the upper part of the Tortonian–Messinian Reef Complex of Mallorca, and both units are regionally topped by an unconformity associated with the Messinian salinity crisis (Fig. 1B and C; Fornós & Pomar, 1983; Pomar *et al.*, 1996; Arenas & Pomar, 2010). The isolation of the studied outcrop makes it difficult to correlate with other sections of the Santanyí Limestone, the closest being coastal cliffs *ca* 5 km to the east (Arenas & Pomar, 2010) and a small road cut near Campos town, *ca* 10 km to the north-west, where the Santanyí Limestone is topped

by Pleistocene deposits (Mas & Fornós, 2006). However, the geographic and topographic position of the studied outcrop, in a relatively high point of the upper Miocene platform, suggest that it corresponds to the topmost deposits of the unit, probably equivalent to 'unit V' of Arenas & Pomar (2010).

The Santanyí Limestone includes diverse and abundant microbialites, but the ones analysed here differ significantly from previously studied examples (Arenas & Pomar, 2010; Suarez-Gonzalez *et al.*, 2019a) in their macro-scale, meso-scale, and micro-scale features, making them unique in the context of the studied unit and intriguing when compared with analogues worldwide.

METHODS

The analysed road cut is 200 m long and up to 4 m high (Fig. 2), on which four stratigraphic sections were logged to assess lateral variations. These sections were measured at centimetre-scale (with more detail on the microbialite biostrome, focus of this study) and were integrated in a single synthetic log *ca* 4.5 m thick (Fig. 3). Twenty-eight samples were collected for laboratory analyses, and polished hand specimens were made from all of them. Polished and uncovered 30 μm thin sections were studied, 16 of 46 x 25 mm and 12 of 50 x 80 mm. The classifications of Dunham (1962) and Choquette & Pray (1970) have been used, respectively, for textural and porosity descriptions of carbonates. Thin sections were studied using standard petrographic techniques and cathodoluminescence. Transmitted-light (TL) and polarized-light (PL) microscopy was carried out using a Nikon Eclipse LV100NPOL (Nikon, Tokyo, Japan). Cathodoluminescence (CL) examination was carried out using a Technosyn® cold cathodoluminescent unit [Cambridge Image Technology Limited (CITL), Hatfield, UK] operating at 14 to 17 kV with 350 to 450 μA beam current. Following examination with CL, half part of each thin section was stained with Alizarin Red S and potassium ferricyanide (Dickson, 1966) for identification of carbonate minerals and estimation of Fe content of calcite. Also, five representative samples (small solid pieces 2 x 5 x 8 mm), were used for scanning electron microscopy (SEM; Carl Zeiss MERLIN™ FESEM; Carl Zeiss AG, Oberkochen, Germany), operating at 3 to 15 kV and 158 pA), at the *Servicios de Apoyo a la Investigación (SAI)* of the University of Zaragoza (Spain). Qualitative chemical element analyses were performed on this SEM with energy-dispersive X-ray spectroscopy (EDS). Bulk sediment X-ray diffraction (XRD) was performed on two samples of

the dark facies. Samples were grounded and sieved to 62 μm and analysed by XRD with a Bragg-Brentano PANalytical X'Pert PRO MPD alpha1 diffractometer (Malvern Panalytical, Almelo, The Netherlands) equipped with a Ge monochromator and CuKα1 radiation, at the *Serveis Cientificotécnics* laboratory of the University of Barcelona and with a D-Max Rigaku diffractometer (Rigaku, Tokyo, Japan) equipped with a graphite monochromator and CuKa radiation, at the *SAI* of the University of Zaragoza.

DESCRIPTION OF MAIN UNITS

The studied outcrop includes five limestone beds, which are laterally continuous throughout the 200 m of the road cut (Figs 2 and 3). The beds are mostly horizontal, with slight undulations <5º, and do not show significant lateral variations (Fig. 2), except for the microbialite biostrome (Bed 2), whose features will be described in detail in the following section. Outcrop conditions are excellent, with local karstification at the base and top of Bed 2 (Figs 2 to 6).

Bed 1 is up to 1.4 m thick, although its base is not visible, and has a flat to slightly-undulated top (Figs 2B, 3 and 4A). It is light-grey to light-beige coloured, mostly massive but with local small-scale cross-bedding (Figs 2B, 4A and 4B). Texture changes from grainstone at the base to packstone at the top. Grainstone components are mainly peloids, with minor micritic ooids, grapestones, bioclasts (mollusc fragments, miliolid foraminifera and ostracods) and *Favreina*-like faecal pellets (Fig. 4C and D; see further description in Bed 5, below). Packstone microfacies are almost exclusively composed of peloids, including minor miliolid foraminifera and ostracods (Fig. 4E). In this bed, primary porosity is filled by a blocky calcite cement, which may occlude pores (Fig. 4C). Mouldic and vug-type secondary porosity may be filled by blocky calcite cement or may remain unfilled (Fig. 4C and D); micrite may be recrystallized to microsparite (Fig. 4F).

Bed 2 is a microbialite biostrome up to 60 cm thick and laterally continuous throughout the whole outcrop (Fig. 2). Its dark colour contrasts with that of the other beds (Figs 2 and 5). Since Bed 2 is the main aim of this study, it will be described in detail in the next section.

Bed 3 is thinly-bedded (centimetre-scale) to nodular, dark-grey in colour, with its thickness (40 to 60 cm) adapting to irregularities of the underlying Bed 2 microbialites, being thinner over domed areas and thicker over troughs and flat areas (Figs 2, 3, 5, 6 and 7). Its internal layering is locally lapping on top of Bed 2 (Figs 5B, 5C and 7B) and its top is a flat to slightly-undulated

contact with Bed 4 (Figs 2, 5 and 6A). The outcrop conditions of Bed 3 are not optimal throughout the road cut (Figs 2C and 6A). Under the microscope, samples of Bed 3 are largely recrystallized and the original components, if present, could not be determined. In detail, they are composed of an alternation of microsparitic layers (up to 2 to 3 mm thick) and pseudosparitic layers (up to 6 mm thick) composed of a xenotopic mosaic of calcite crystals, with cloudy appearance (Fig. 6C).

Bed 4 is 0.8 to 1.0 m thick, grey in colour and massive to crudely-bedded, with flat to slightly-undulated base and top (Figs 2, 3, 5 and 6). The lower part has a grainstone texture with peloids, *Favreina*-like faecal pellets (see further description in Bed 5, below), foraminifera and moulds of gastropods and bivalve shells. The upper part is a peloidal packstone with scattered ostracods, also including subrounded lighter patches with less micrite, *ca* 1 mm in diameter, probably representing bioturbation (Fig. 6D). Primary intergranular porosity in grainstone facies is partially filled by an isopachous rim of non-ferroan calcite cement, which also fills secondary mouldic and vug-type porosity (Fig. 6F). This calcite cement may be post-dated, commonly after a corrosion surface, by non-ferroan blocky calcite cement. Nevertheless, porosity remains commonly unfilled (Fig. 6F).

Bed 5 is light-grey to light-beige in colour, has a flat to slightly-undulated base, and its top is not visible due to recent erosion, being up to 1.2 m thick (Figs 2, 3, 5 and 6). It mostly consists of massive packstone with abundant millimetre-scale elongated to subrounded grainstone patches that may represent bioturbation (Fig. 6E). The main components are irregular micritic peloids and faecal pellets, recognized as elongated micritic grains with small longitudinal cement-filled canals, equivalent to the *Favreina* ichnogenus of crustacean faecal pellets (Fig. 6E; cf. Dondi & Papetti, 1966; Kennedy *et al.*, 1969; Schweigert *et al.*, 1997; Knaust, 2020). Less abundant components are poorly-preserved ooids, ostracods and miliolid foraminifera. As in Bed 4, an isopachous rim of non-ferroan calcite cement partially fills primary intergranular porosity of the grainstones (Fig. 6G), as well as secondary mouldic and vug-type porosity. This calcite cement is occasionally postdated by scattered opaque minerals (see subsection on the dark colour of Bed 2, below) and/or by non-ferroan blocky calcite cement, which may post-date a corrosion surface (Fig. 6G). Most larger pores remain unfilled after precipitation and corrosion of the isopachous cement.

DETAILED DESCRIPTION OF THE MICROBIALITE BIOSTROME

The conspicuously dark-coloured microbialite biostrome of Bed 2 is relatively thin (up to 60 cm) and laterally continuous throughout the outcrop (Figs 2 and 5), but with a significant lateral and vertical variability at macro-scale, meso-scale and micro-scale (Figs 7 to 14). The morphology of the biostrome is overall flat but with gentle domes, <50 cm thick and *ca* 1 m wide (Figs 2, 5, 6A and 7). Its base and top are irregular (Figs 2 and 5), the top being an erosion surface (see below, *Level 2d*; Figs 5B, 7A and 7B). Troughs between the biostrome domes are filled by cross-bedded grainstone and/or by flat-pebble breccia of black, grey and white intraclasts (Figs 5B, 7A and 7B). Although the dark-grey colour is distinctive, internal heterogeneities are observed: four laterally-variable levels of contrasting colour and texture have been differentiated from base to top (*Levels 2a–2d*; Figs 3 and 7).

Level 2a

Locally, the base of the biostrome is a thin level (<5 cm), dark-grey to black, cross-laminated, and with minimal lateral continuity, <1 m (Figs 5A, 7C and 7E). It consists of oolitic–peloidal grainstone with minor bioclasts (ostracods and miliolid foraminifera).

Level 2b

On top of the thin, dark, grainy level, a light-grey to white level occurs (Figs 5A, 5B and 7A to E). This level is laterally more continuous than the underlying one, and it typically forms the base of the biostrome; its thickness ranges from 2 to 15 cm, being thicker at the central parts of the biostrome domes (Fig. 7A, C and E). This level exhibits an irregular to domed shape, with flat to undulated base and undulated convex top, and its appearance is commonly massive, although locally faintly laminated (Fig. 7A, C and E). Under the microscope, the most common internal structure is a submillimetric lamination composed of alternating dense-micritic and clotted-peloidal laminae (Fig. 8A to C). Within this lamination, shrubby structures occur, up to 5 mm wide and tall, unfilled or filled with non-ferroan calcite (Fig. 8A and C). Erect and branching tufts, up to 5 mm tall, made of micritic or pseudosparitic filaments grouped in microdomes up to 7 mm wide also occur (Fig. 8E). These internal structures are cut, deformed and disrupted by irregular surfaces, commonly with subrounded borders, which generate irregular tubes or cavities, several centimetres long, without a preferential orientation, ranging from perpendicular to parallel to

lamination (Fig. 8). These tubes or cavities do not show a mineralized wall and are filled by small peloids (50 to 200 μm in diameter) embedded in an open fabric of clotted-peloidal micrite with abundant calcite cement (Fig. 8).

Level 2c

This is the thickest (15 to 30 cm) and most conspicuous level of the biostrome, due to its dark colour and its lateral continuity (Figs 2B, 5 and 7). It is divided in two different parts: a thinner lower one, and a thicker upper one (Fig. 7A, D, E and F).

Thinner lower part

The thinner lower part of Level 2c is 1 to 5 cm thick and consists of grainy black deposits with abundant white vertical dendritic structures, up to 1 cm wide and 5 cm tall, which typically branch and widen upward, forming tufts (Figs 7A, 7E to 7G, 9A and 9C to 9E). Petrographically, the grainy deposits consist of oolitic–peloidal grainstone, with minor bioclasts (ostracods, miliolid foraminifera and small mollusc fragments), and abundant opaque minerals (see subsection on the dark colour of Bed 2, below) that produce the characteristic black colour (Fig. 9A, B, C and E). Contrarily, the vertical dendritic structures only include minor traces of these opaque minerals and thus show white colour (Figs 7G and 9). Under the microscope, the dendritic structures consist of vertical branching microcolumns, 0.5 to 3.0 mm wide (Fig. 9A, C and D). Internally, these microcolumns show a recrystallized clotted-peloidal micritic fabric with faint relicts of convex lamination (Fig. 9C to E). This clotted-peloidal fabric includes only rare and sporadic allochthonous grains, and it has abundant sparitic calcite cement filling porosity, which produces the lighter colour under the microscope (Fig. 9E). The contact between the microcolumns and the adjoining grainstone is overall subvertical, although very irregular, and it does not show a mineralized wall (Fig. 9).

Thicker upper part

The thicker upper part of Level 2c is 15 to 25 cm thick and has two contrasting structures: laminated and columnar (Fig. 10).

Laminated structure: This is less abundant, and where it occurs, it grades vertically and laterally to the columnar structure (Fig. 10A and C). It consists of alternating darker and lighter laminae with an even shape and a flat to slightly convex geometry. The colour difference between laminae is usually inconspicuous and produces a faint macroscopic lamination (Fig. 10). Locally, small (<1 cm wide and deep) concave subrounded cavities disrupt the lamination at the top, being filled by the black overlying sediment (Fig. 10D). Within one of them, a fossil cast of a mollusc, probably a gastropod, occurs (Fig. 10F). Under the microscope, the laminated structure consists of alternating thick (<4 mm) light laminae and thinner (<2 mm) dark laminae (Fig. 11). Dark laminae have a dense-micritic to clotted-peloidal fabric, whereas light laminae have an open clotted-peloidal micritic fabric, often arranged in filamentous structures perpendicular to lamination, and with relatively large (up to 3 mm wide) irregular to shrub-shaped pores filled with sparitic calcite cement (Fig. 11). Very few allochthonous grains occur within the laminae (Fig. 11). Very locally, a finely laminated and slightly domed microstructure, with laminae <100 μm thick and domes <2 mm wide and tall, also occurs (Fig. 11C).

In transitional zones between laminated and columnar structure, incipient black intercolumn spaces are observed (Fig. 10A and C). These spaces have highly irregular borders and typically are subvertical, although they locally curve and show subhorizontal orientation (Fig. 11C and D). They are filled with oolitic–peloidal grainstone rich in opaque minerals (see further descriptions below). Irregular millimetric patches filled with dark oolitic–peloidal grainstone or calcite cement are also observed disrupting the laminated structures, and locally they are connected to the intercolumn spaces (Fig. 11A and C). Locally, where weathering has exposed the upper surface of a transitional zone between laminated and columnar structures, the incipient black intercolumn spaces are seen in plan view as elongated traces, *ca* 1 cm wide, with an irregular to subpolygonal distribution and rounded edges resembling *Thalassinoides* that penetrate downward (up to 10 cm) keeping the same size and shape in depth (Figs 10E and 11C).

Columnar structure: This is the most common structure in this level and it consists of grey vertical columns, 0.5 to 2.5 cm wide and up to 20 cm tall, separated by black intercolumn space typically narrower than the columns (<1 cm wide), although it locally reaches up to 4 cm wide (Figs 7 and 10). The internal structure of the columns is not clear at the outcrop or in hand specimen, although it locally reveals faint convex lamination (Fig. 10A and C). The intercolumn space has a more evident internal structure, with abundant concave laminae (Figs 7, 10A and

10C). Columns commonly individualize upward from a basal, laterally continuous laminated level (Figs 7D to 7G, 10A and 10C). Most columns are branching, often splitting in two, some widening upward, but most of them maintain a constant width (Figs 7D to 7G and 10C). Locally, a sharp horizontal interruption of the columns occurs at the middle part of the biostrome, onto which new columns develop (Fig. 7F). The contact between columns and intercolumn space is generally irregular, only locally straight, and with an overall subvertical trend, but locally it curves and is even subhorizontal (Figs 7E to 7H and 10A to 10C). Grey bridges often join adjacent columns, crossing the intercolumn space (Fig. 10A and C). The upper surface of this columnar structure, where visible, exposes a very irregular distribution of columns and intercolumn space, with no particular pattern or orientation (Fig. 10B). The intercolumn space is filled by oolitic–peloidal grainstones, with minor bioclasts (ostracods, miliolid foraminifera and small mollusc fragments), and with abundant opaque minerals (see subsection on the dark colour of Bed 2, below) that produce the characteristic black colour (Figs 12 and 13). Under the microscope, the columns have faint traces of convex lamination and include fewer opaque minerals, which produces their lighter appearance (Figs 12 and 13). Internally, columns consist of an open fabric of thin elongated threads of clotted-peloidal micrite, which have an irregular to sub-reticulate arrangement, limiting relatively large (up to 5 mm wide), sparite-filled, irregular to shrub-shaped pores (Figs 12 and 13). Fan-like or tufted filamentous structures are common but poorly-preserved (Figs 12 and 13). Very few allochthonous grains occur within the columns (Figs 12B and 13), but irregular millimetric patches filled with dark oolitic–peloidal grainstone occur (Fig. 12A). The contact between the columns and the intercolumn space is very irregular under the microscope, and it often curves, locally being even subhorizontal (Fig. 12A). A thin (<500 μm), discontinuous, micritic wall occurs at some parts of the boundary between columns and intercolumn space (Fig. 13B).

Level 2d

The uppermost level of the biostrome is discontinuous due to the erosive contact with the overlying Bed 3 (Figs 5B, 7A and 7B). Where it occurs, it is 5 to 15 cm thick, light-grey in colour, and typically massive with only local traces of lamination (Fig. 7A to D). Under the microscope, this level is partially altered by diagenesis (Fig. 14A). Where better preserved, very thin (<300 μm) alternating laminae of dense micrite and clotted-peloidal micrite are visible (Fig. 14B). This lamination is locally displaced by shrubby structures and small (<700 μm long) pseudomorphs

after subhedral minerals, hollow or filled with calcite cement (Fig. 14B). In recrystallized areas, it is hard to identify the original components and textures, although calcite pseudomorphs, up to 5 mm long, after probable euhedral evaporite minerals are observed, as well as traces of fenestral porosity (Fig. 14A).

The dark colour of Bed 2

A remarkable and striking feature of Bed 2 is its dark colour, which contrasts with the light-beige or grey colours of the underlying and overlying beds (Figs 5 and 7). In detail, the darker areas correspond to the oolitic and peloidal (grainy) facies observed in Level 2a and between the dendritic and columnar microbialite structures of Level 2c (Figs 7, 10, 11, 12 and 13). In turn, these microbialite structures of Level 2c show a dark-grey colour, which also contrasts with the lighter colour of microbialites of Levels 2b and 2d (Fig. 7).

Under the microscope, the micritic components, such as ooids and peloids, are commonly opaque under transmitted-light (TL) microscopy (Figs 9, 11 to 13, 15A and 15B). Under TL, SEM and BSEM, an opaque mineral is observed replacing partially or totally these components and, locally, also the clotted-peloidal micrite of the microbialite (Fig. 15A to D). The EDS coupled with the electron microscope indicates that the opaque mineral or minerals correspond to manganese oxyhydroxides (Mn Ox/Hx). However, despite the evident dark colour of this bed, mineral concentration is below the analytical resolution of the X-ray diffraction equipment, and thus it was not possible to determine the specific mineralogy.

The Mn Ox/Hx also occur as: (i) a thin rim surrounding and partially filling primary porosity (Fig. 15A and D); (ii) a thin rim surrounding the contact between the grainy facies and the microbialites (Fig. 15A and B); and (iii) around the border of the mouldic and/or vug-type secondary porosity (Fig. 15E). However, in microbialites the occurrence of Mn Ox/Hx in mouldic porosity, created after complete decay of organic matter (see further discussion below), is scarce (Figs 8C, 9A, 9C, 9D, 9E, 11A, 11B, 12, 13 and 15B). Precipitation of Mn Ox/Hx is postdated by precipitation of non-ferroan and non-luminescent blocky calcite cement, which commonly occludes porosity (Fig. 15A, B and E to I). Locally, a thin, euhedral and bright-orange luminescent zone, with brownish-orange colour under TL microscopy, occurs between non-luminescent zones (Fig. 15F and G). Where Mn Ox/Hx are not present, primary and secondary mouldic and vug-type

pores are filled by non-ferroan and non-luminescent blocky calcite cement (Fig. 15J and K), identical to that observed where Mn Ox/Hx are present.

In Levels 2b and 2d, as well as in Beds 1, 3, 4 and 5, Mn Ox/Hx are much less abundant, but still present as small patches replacing micritic matrix and components, and, scarcely, partially filling primary and secondary porosity (Figs 6F and 14B). In these beds, like in Levels 2a and 2c, precipitation of Mn Ox/Hx is post-dated by non-ferroan and non-luminescent blocky calcite cement and, locally, in Beds 4 and 5, it is pre-dated by isopachous calcite cement (Fig. 6G).

DISCUSSION

Sedimentological and geomicrobiological interpretations

General sedimentological setting

The sedimentological and palaeontological characteristics of the studied deposits indicate that they were formed in a shallow marine environment that was, at least temporarily, restricted, as suggested by the lack of open-marine fossils (for example, corals and echinoderms) and predominance of ostracods, miliolids and molluscs. This interpretation is consistent with the general depositional setting of the Santanyí Limestone, formed by intertidal microbialites and palaeosols (i.e. mangroves) with low diversity biota, and subtidal oolitic grainstones with giant microbialites and, where present, bioclasts with low abundance and diversity (Fornós & Pomar, 1983; Pomar *et al.*, 1996; Arenas & Pomar, 2010; Suarez-Gonzalez *et al.*, 2019a). The Santanyí Limestone is coeval with the Tortonian–Messinian Reef Complex, and although the exact relationship between these two units does not crop out, their current geographic locations and their stratigraphic analysis have allowed to assign the Santanyí Limestone to the inner part of a shallow-water platform associated to some Messinian reefs (Pomar *et al.*, 1996; Arenas & Pomar, 2010).

The dominant facies in the outcrop studied here are peloidal–oolitic packstone and grainstone (Beds 1, 4 and 5), identical to other localities of the unit (Arenas & Pomar, 2010; Suarez-Gonzalez *et al.*, 2019a), indicating a shallow and agitated depositional environment. Furthermore, *Favreina* faecal pellets are also common, which means that bioturbation was significant, probably associated with *Thalassinoides*-forming crustaceans (e.g. Kennedy *et al.*, 1969; Sellwood, 1971). Although *Thalassinoides* traces are not evident in the packstone–

grainstone facies of the studied outcrop, they are common in other outcrops of the unit (Suarez-Gonzalez *et al.*, 2019a), and potentially similar traces occur in the biostrome of Bed 2 (Fig. 10E; see further discussion below). Therefore, the overall depositional setting is envisaged as the inner part of a large shallow-water platform, where sediments were frequently swept by currents (for example, waves and storms) and disrupted by burrowing animals (cf. Arenas & Pomar, 2010; Suarez-Gonzalez *et al.*, 2019a). These depositional conditions would resemble those of some modern Bahamian lagoons and banks (e.g. Purdy, 1963a,b; Reijmer *et al.*, 2009).

The remarkable lateral continuity of the biostrome of Bed 2 (Fig. 2) suggests that an environmental variation occurred within the system, inducing the widespread emplacement of microbial-dominated conditions. Similar shifts to extensive microbialite development have been interpreted, in the same unit, as triggered by environmental changes (Arenas & Pomar, 2010; Suarez-Gonzalez *et al.*, 2019a). In the studied outcrop, there is evidence of an increase in water restriction and salinity during deposition of Beds 2 and 3: (i) the decrease in bioclast abundance and diversity in both beds; (ii) the presence of evaporite moulds in Level 2d (Fig. 14A); and (iii) the occurrence in Bed 3 of layers with pseudosparitic fabric, composed of a xenotopic mosaic of cloudy calcite crystals (Fig. 6C), which is interpreted as the result of calcitization of evaporites in meteoric settings, via flushing of groundwaters undersaturated in $CaSO_4$ and supersaturated in $CaCO_3$ (cf. Pierre & Rouchy, 1988; Quijada *et al.*, 2014; Warren, 2016). Beds 4 and 5 marked the return to less restricted peloidal–oolitic deposition, characteristic of many intervals of the Santanyí Limestone (Arenas & Pomar, 2010).

Development of the microbialite biostrome of Bed 2

Despite the lateral continuity of the microbial biostrome of Bed 2, it contains remarkable internal heterogeneities, induced by a succession of accretion episodes. Small, rippled oolitic–peloidal deposits developed locally first (dark-coloured Level 2a) and were overlain by laterally-extensive low-relief microbialite domes (white Level 2b; Figs 3, 5 and 7). These microbialite domes were dominated by laminated structures (Fig. 8; i.e. stromatolites, *sensu* Riding, 1999; Bosak, 2013) with scattered shrubby millimetric bodies that could represent moulds of mat microbes (Fig. 8A and C; cf. Suarez-Gonzalez *et al.*, 2019a). The less common tufted filamentous microstructure (Fig. 8E) could also represent calcified filamentous microbes. The ubiquitous irregular and elongated, centimetre-wide spaces that pervasively disrupt lamination in Level 2b

(Fig. 8) are very similar to centimetre-scale invertebrate bioturbation galleries commonly observed in carbonate sediments (cf. Kennedy, 1975; Tucker & Wright, 1990; Demicco & Hardie, 1994; Scholle & Ulme-Scholle, 2003; Flügel, 2010; Knaust *et al.*, 2012; Buatois & Mángano, 2013). As in these cited examples, the spaces are often filled by small peloids, which are likely faecal pellets of the trace-makers. Thus, despite the absence of bioclasts (i.e. absence of organisms with calcified skeletons in the original environment, probably due to increased restriction and salinity, as discussed above), environmental conditions allowed some non-calcified invertebrates to thrive and colonize the sediment, as described in other ancient examples where biotic stress was caused by high or low salinity (Quijada *et al.*, 2013; 2020; Quijada, 2014; Campos-Soto *et al.*, 2017; 2019). In addition to invertebrates, large green algae such as *Acetabularia* are also responsible for bioturbation in modern microbialites (cf. Reid *et al.*, 2011), similar to some of the smaller cavities observed in Level 2b.

The main development phase of the biostrome corresponds to the dark-coloured Level 2c, which started with peloidal–oolitic deposition, especially in the troughs between domes of Level 2b (Fig. 7A and E), coeval with the growth of small, laminated, dendritic tufts, which developed over the higher part of the domes, forming millimetre to centimetre-scale branching columns (Figs 7E to 7G and 9). These are interpreted as the product of accretion of spatially localized benthic microbial communities that grew upward, with low synoptic relief, and simultaneously with grain accumulation between columns, in accordance with other examples of similar small dendritic microbialite columns in grainy settings (e.g. Ezaki *et al.*, 2017; Suosaari *et al.*, 2018). Very scarce grains occur within the laminated microstructure of the tufts (Fig. 9), implying that they accreted through early mineralization of the microbial community, rather than trapping and binding of the surrounding particles (cf. Suarez-Gonzalez *et al.*, 2019b, and references therein). Over this thin dendritic and grainy level, the most conspicuous part of the biostrome developed as wide and gentle dark-coloured domes of laminated and columnar microbialites (Figs 5, 7 and 10).

Peloidal–oolitic grainstone occurs in the intercolumn space and between laminated parts of Level 2c, but only rare and small peloids are observed within the microbialites. Thus, the primary accretion process was early mineralization of the benthic microbial communities, although accretion was probably simultaneous with grain accumulation (cf. Suarez-Gonzalez *et al.*, 2019b, and references therein). Lamination is faint but evident in some parts of the microbialite, being classifiable as stromatolites (*sensu* Riding, 1999; Bosak, 2013). Classification of the columnar

parts is not straightforward since, macroscopically, they only contain traces of convex lamination, but they are not composed of mesoscopic clots, characteristic of thrombolites (*sensu* Kennard & James, 1986; Shapiro, 2000). However, both columnar and laminated structures appear quite similar under the microscope, suggesting that both shared similar accretion processes, which is further supported by the gradual lateral and vertical transition between both structures (Figs 10A, 10C and 11C). These microstructures mainly consist of open frameworks of clotted-peloidal micrite, which is widely interpreted to be the result of organomineralization during the degradation of organic matter (including extracellular polymers, EPS) within microbial communities (e.g. Chafetz & Buczynski, 1992; Reitner, 1993; Arp *et al.*, 1998; Dupraz *et al.*, 2004; Riding & Tomás, 2006). Here, clotted-peloidal micrite is typically arranged in elongated threads with filamentous to sub-reticulate shapes, locally forming fan-like or tufted morphologies (Figs 11, 12 and 13), probably representing mineralized remains of mat microbes. These clotted-peloidal microstructures often limit centimetre-scale irregular to shrub-shaped pores, (Figs 11B, 12 and 13), similar to those interpreted as unmineralized areas of the microbial mat in other examples (cf. Reitner, 1993; Riding & Tomás, 2006; Suarez-Gonzalez *et al.*, 2019a). This interpretation is plausible, given that organic matter in some parts of modern microbial mats can remain locally unaltered for long periods, even millennia (e.g. Brook *et al.*, 2011; Blumenberg *et al.*, 2015; Shen *et al.*, 2018; 2020). After final decay of the unmineralized organic matter, mouldic pores might be subjected to diagenetic alteration, including dissolution, enlargement and cement precipitation (see the section on the interpretation of diagenetic aspects, below).

Concave subrounded cavities at the top of laminated parts of Level 2c are interpreted as evidence of metazoan bioturbation (Fig. 10D and F). An erosive origin is discarded due to their chamber-like shape and to their very local occurrence. Their outline cuts lamination (Fig. 10D), suggesting that the microbialite substrate was partially lithified or at least firm, thus making them classifiable as borings, rather than burrows. In addition, their chamber-like shape resembles that of *Gastrochaenolites* borings (e.g. Akpan, 1991; Cónsole-Gonella *et al.*, 2009; Föllmi *et al.*, 2011). Equivalent metazoan bioerosion is common on the top surface, and after partial lithification, in modern shallow-marine microbialites of Bahamas (Riding *et al.*, 1991; Andres & Reid, 2006) and Shark Bay, Australia (Jahnert & Collins, 2011; 2013), and has also been described in some fossil examples (Hasiotis, 2004; Rodríguez-Martínez *et al.*, 2012).

The columnar parts of Level 2c include evidence of being an original accretionary structure, but also features suggestive of bioturbation, both in section and in plan view (Figs 10 to 13). Therefore, interpretation of their accretion history is not univocal, posing questions about the role of metazoan disruption, which will be addressed in detail in the next subsection.

The final stage of biostrome development corresponds to light-coloured Level 2d, locally poorly preserved due to diagenetic alteration and erosion (Figs 5, 7 and 14). Where preserved, it has stromatolitic internal structure (i.e. laminated microbialite, *sensu* Riding, 1999; Bosak, 2013), and inherits the domal shape of underlying Level 2c. It accreted through mineralization of benthic microbial communities, probably in the absence of coeval grainy sediments and under evaporitic conditions, as attested to by pseudomorphs after evaporites (Fig. 14; see further discussion above). After deposition, the biostrome underwent erosion and flat pebbles of both dark-coloured and light-coloured levels were deposited as breccia in the troughs between microbial domes (Figs 5B, 7A and 7B). Sedimentation resumed under probable evaporitic conditions with Bed 3 (see further discussion above).

Morphogenesis of columnar microbialites: constructive, destructive or both?

Level 2c of the studied microbialite biostrome is dominated by centimetre-scale wide and decimetre-scale tall branching subcylindrical columns separated by oolitic–peloidal grainstone. This structure was ubiquitous in Proterozoic stromatolites (e.g. Awramik, 1971; Bertrand-Sarfati, 1972; Walter, 1972; Cao, 1988; Grotzinger & Knoll, 1999), and it seems somehow anachronistic for the Miocene because columns became smaller and rarer in Phanerozoic microbialites, especially after the Cambrian (e.g. Walter, 1972; Monty, 1973; Awramik & Sprinkle, 1999). Proterozoic columnar stromatolites (and their rare Phanerozoic counterparts) have varied sizes and shapes, as well as internal structures (e.g. Awramik, 1971; Hoffman, 1976a; Grotzinger & Knoll, 1999; Raaben, 2006), but their columns are consistently interpreted as the result of vertical accretion of spatially localized benthic microbial communities. The resulting laminae in the columns had low synoptic relief due to continuous current scouring and interaction with the interstitial sediment (e.g. Grotzinger & Knoll, 1999; Dupraz *et al.*, 2006; Bosak *et al.*, 2013; Tosti & Riding, 2017; Martin-Bello *et al.*, 2019). The columns of the studied Miocene biostrome are macroscopically very similar to some Proterozoic examples, with some characteristics suggesting that columns were accretionary structures: (i) the presence of microbialite bridges repeatedly

joining adjacent columns (Figs 7F, 10A and 10C); (ii) the occurrence within the columns of scarce and scattered grains equivalent to those in the intercolumn space (Figs 12 and 13); and (iii) the presence of scarce and faint convex laminae in the columns (Figs 12 and 13).

However, the studied Miocene columns show other aspects that differ from many Proterozoic examples (Fig. 16) and that are not likely to be microbial accretionary features: (i) the highly irregular boundaries between columns and intercolumn space (Figs 7H, 10A, 10C, 11, 12 and 13); (ii) the fact that this boundary commonly seems to cut the internal structures of the columns (Figs 11 to 13); (iii) the sporadic occurrence and irregular distribution of a mineralized wall of the columns, which also seems to cut their internal structures (Figs 12 and 13); (iv) the common oblique and subhorizontal attitude of the intercolumn space in section (Figs 11 and 12); and (v) the fact that in plan view the intercolumn space does not show a regular pattern, but rather an irregular network of intersecting and/or diverging galleries (Fig. 10E). Concerning this last point, those galleries are here interpreted as *Thalassinoides*-like traces due to their three-dimensional structure and the fact that they penetrate downward keeping the same size and shape in depth (Fig. 10E), being very similar to structures interpreted as *Thalassinoides* in other examples associated with microbialites (cf. figs 5c and 7 of Sprechmann *et al.*, 2004; and fig. 8 of Masari & Westphal, 2011). The aforementioned aspects seem to be destructive, rather than constructive, and are largely comparable with typical features and structures of bioturbation in carbonate rocks (cf. Kennedy, 1975; Tucker & Wright, 1990; Demicco & Hardie, 1994; Scholle & Ulme-Scholle, 2003; Flügel, 2010; Knaust *et al.*, 2012; Buatois & Mángano, 2013). Thus, it is interpreted here that the studied Miocene columns are microbialite structures formed not solely by the accretion of benthic microbial communities, but also influenced by the interaction with, and disruption by, bioturbating organisms, most likely metazoans.

Bioturbation has long been regarded as antagonistic with microbialite development since it was first proposed that the late Proterozoic decline in microbialite abundance and diversity was due to the appearance of grazing and burrowing metazoans (Garrett, 1970; Awramik, 1971; Walter & Heys, 1985). This hypothesis has been largely debated (e.g. Monty, 1973; Pratt, 1982; Cao, 1988) and, although parts of it remain plausible, it is now accepted that many other environmental and ecological factors besides metazoan disruption concurred to produce the Proterozoic decline of stromatolites, and the variations in microbialite abundance and diversity of the Phanerozoic (e.g. Grotzinger, 1990; Riding, 2006; 2011). In fact, bioturbation is relatively common in some

Phanerozoic microbialite-bearing settings: i.e. burrowed Cambrian–Ordovician thrombolites (e.g. Aitken, 1967; Radke, 1980; Kennard, 1994; Glumac & Walker, 1997; Harwood Theisen & Sumner, 2016); mud mounds, microbial–metazoan reefs, and even microbialite components of modern reefs (e.g. Reitner, 1993; Shen & Webb, 2005; Rodríguez-Martínez, 2011, and references therein; Tomás *et al.*, 2013; Rodríguez-Martínez & Reitner, 2015); marine hardgrounds, condensed sequences and hiatal surfaces (e.g. Föllmi *et al.*, 2011; Massari & Westphal, 2011); and freshwater microbialites and tufas with insect larvae (e.g. Bertrand-Sarfati *et al.*, 1994; Drysdale, 1999; Hägele *et al.*, 2006; Arenas *et al.*, 2007; Gradziński, 2010). However, bioturbation within most Phanerozoic microbialites is still rarely described (see exceptions in the references of next paragraph), although its presence in modern microbialites is starting to be more recognized (see literature reviews in Farmer, 1992; Tarhan *et al.*, 2013; Cónsole-Gonella & Marquillas, 2014; Rishworth *et al.*, 2016).

Given the potential role of bioturbation in shaping the studied Miocene columnar microbialites, an essential question is how and when the bioturbation was produced. Two possible answers are: (i) that bioturbation occurred once microbialite accretion had finished; or (ii) that bioturbation was contemporaneous with microbialite development. Post-accretionary destruction of microbialites by bioturbating organisms is observed in modern examples (Riding *et al.*, 1991; Andres & Reid, 2006; Jahnert & Collins, 2011; 2013) and has been described in a few fossil specimens (Hasiotis, 2004; Rodríguez-Martínez *et al.*, 2012). This post-accretionary bioerosion was probably produced in the concave borings at the top of the laminated parts of Level 2c (Fig. 10D and F), but it cannot fully explain some key features of the studied columnar structure: (i) the common microbialite bridges joining adjacent columns (Figs 7F, 10A and 10C), which indicate phases of laterally continuous microbial growth, not disrupted by bioturbation and not restricted to the columns; (ii) the scarce presence within columns of scattered grains equivalent to those of the intercolumn space (Figs 12 and 13), pointing to coeval column growth and intercolumn grainy sedimentation; and (iii) the highly irregular boundaries between columns and intercolumn space (Figs 7H, 10A, 10C, 11, 12 and 13), which suggest that bioturbation took place probably before complete lithification of the benthic microbial communities. These features indicate that, in the studied example, bioturbation was simultaneous with, and/or occurred very soon after, microbialite accretion. In this regard, recent studies are starting to show that epifaunal and infaunal bioturbators are more active during microbialite development than previously thought, and in different modern settings including continental (Garcia-Pichel *et al.*, 2004), coastal (Rishworth *et*

al., 2016; 2019) and marine environments (Andres & Reid, 2006; Planavsky & Ginsburg, 2009; Jahnert & Collins, 2011; 2013; Tarhan *et al.*, 2013). Similarly, in most of the few fossil examples of bioturbated microbialites, bioturbation is interpreted as simultaneous with microbial accretion (Wright & Mayall, 1981; Ekdale, 1989; Akpan, 1991; Lamond & Tapanila, 2003; Druschke *et al.*, 2009; Cónsole-Gonella & Marquillas, 2014; Bourillot *et al.*, 2020), which proves that the relationships between benthic microbial communities and their bioturbators are not limited to destruction and exclusive competition. Moreover, in some cases, bioturbation may have had a significant, although cryptic, role in the development and fossilization of microbialite structures (Wright & Mayall, 1981; Ibarra *et al.*, 2014; Suarez-Gonzalez *et al.*, 2019c; Quijada *et al.*, 2020).

In summary, the Miocene columnar microbialites studied here are interpreted to result from a combination of microbial accretion and epifaunal and infaunal bioturbation, which co-occurred in a restricted shallow-water platform, probably with salinity higher than normal-marine. Interestingly, Farmer (1992) presented some modern environments where microbial mat bioturbation is stronger in areas with relatively high salinity and with irregular mat surfaces. This scenario is very plausible for the studied microbialites, with columns representing mat zones with a slight synoptic relief over the rest of the surface. In fact, most models proposed to explain the morphogenesis of columnar microbialites (e.g. Grotzinger & Knoll, 1999; Dupraz *et al.*, 2006; Bosak *et al.*, 2013) show that individualization of columns starts when there are localized disruptions on the surface of the microbial community, typically current scouring or grain input. Here, it is proposed that grazing or burrowing could act as a similar disruptive mechanism, inducing the development of spatially disconnected mats that produce microbialite columns: areas more grazed or burrowed do not accrete as much as the undisrupted ones, generating an initial low relief, which may be filled by peloidal–oolitic sediment (some of the peloids may even be faecal products of the bioturbators). The simultaneous continuation of these processes (accretion in the higher areas – future columns – and bioturbation and grain accumulation in the lower areas – future intercolumn spaces), together with the early lithification of the microbial communities, would eventually produce the studied Miocene columnar microbialites (Fig. 16). Therefore, this case study poses a new bioturbation-influenced model for the morphogenesis of columnar microbialites. Descriptions of equivalent bioturbated columns are very rare, except for Upper Proterozoic examples from China (Cao, 1988). Bioturbated microbial laminites in Ordovician siliciclastic settings from USA (Druschke *et al.*, 2009) developed similar columnar structures, although in a different setting, and the arborescent structure of Triassic microbial carbonates from

the UK was also influenced by bioturbation (Wright & Mayall, 1981). These examples pose the question of whether the model proposed here, based on concurrent accretionary and disruptive processes, is uniquely anecdotal or more widespread than previously thought (Fig. 16). The described Miocene case study provides the starting point to test this model in other Phanerozoic microbialites with columnar morphologies, but the occurrence of Proterozoic analogues suggests that it may have been functioning even since the evolutionary dawn of bioturbating metazoans.

On the dark colour of microbialites and the origin of Manganese oxyhydroxides: hypotheses for the future

The overall and characteristic black colour of the studied microbialite biostrome is produced by the presence of Mn Ox/Hx. These minerals are more abundant in Bed 2, but they occur throughout the whole outcrop, indicating that they precipitated after deposition. Moreover, and as discussed below, petrographic features suggest that they precipitated during the relatively early phases of diagenesis, related to the subaerial exposure and meteoric diagenesis of the Santanyí Limestone.

Manganese Ox/Hx are more abundant in the grainy facies than in microbialites. They replace, partially or totally, the micritic components (ooids and peloids) and locally the micritic matrix and microbialites (Figs 11C, 14B and 15A to 15D). They also occur as a thin rim surrounding the boundary between columns and intercolumn space (Figs 11D and 15A). Additionally, Mn Ox/Hx are observed partially filling primary and secondary porosity, post-dating isopachous calcite cement and the corrosion surface that developed subsequently (Fig. 6F). The formation of the mouldic and vug-type porosity and the precipitation of non-ferroan isopachous calcite cement commonly occur in marine sediments during meteoric diagenesis, when the input of undersaturated and relatively acidic freshwater provokes dissolution of the unstable aragonite and high magnesium calcite (Bathurst, 1975; James & Choquette, 1990b; Tucker & Wright, 1990, Scholle & Ulmer-Scholle, 2003). Thus, precipitation of non-ferroan isopachous calcite cement occurred after development of secondary porosity, once the water became supersaturated in calcite; the subsequent and local development of the corrosion surface would have occurred when the meteoric waters became undersaturated again. Another process that probably occurred associated with the meteoric diagenesis is neomorphism and recrystallization of micrite, commonly composed of high-magnesium calcite and/or aragonite, which turned into low

magnesium calcite (Bathurst, 1975; James & Choquette, 1990; Tucker & Wright, 1990, Scholle & Ulmer-Scholle, 2003).

When precipitating in both primary and secondary porosity, Mn Ox/Hx commonly occur as a thin rim surrounding the border of these pores (Fig. 15A, D and E) in both the grainy and the microbialite facies, implying that they precipitated after partial or, less commonly, total dissolution of these components. Nevertheless, in microbialites, mouldic porosity generated by the decay of remaining organic matter contains very scarce Mn Ox/Hx (Figs 8C, 9A, 9C, 9D, 9E, 11A, 11B, 12, 13 and 15B), while they are more abundant in the vug-type porosity (Fig. 15E). Manganese Ox/Hx are post-dated by precipitation of non-ferroan and non-luminescent blocky calcite cement, which may occlude remaining porosity (Fig. 15). Calcite cement probably precipitated in a meteoric phreatic setting and under oxic conditions, as suggested by its petrographic features, its lack of Fe content and absence of luminescence (e.g. James & Choquette, 1990; Tucker & Wright, 1990; Machel & Burton, 1991). The thin and euhedral rim with bright orange luminescence, which locally occurs between non-luminescent zones (Fig. 15F and G), is interpreted as precipitated under sub-oxic conditions, in which Mn is reduced and may be incorporated into the calcite lattice (Machel & Burton, 1991).

Dark-coloured deposits of the Santanyí Limestone are not only observed in the studied outcrop. Similar dark carbonate facies occur in the uppermost part of the Miocene deposits in other areas of Mallorca (the Marratxí, Muro, Santanyí and east of Llucmajor platforms; see Fig. 1). Overall, these dark carbonate facies are informally named "Pont d'Inca Facies" and are thought to be diagenetic in origin, commonly associated with stromatolites and related to hypersaline environmental conditions (Pomar *et al.*, 1983; Mas & Fornós, 2006; Mas, 2015). An erosive surface occurs at the top of the "Pont d'Inca Facies" in several areas of Mallorca, previous to the deposition of Pliocene deposits, which, in turn, may include cobbles and boulders of the dark facies (Mas, 2015), reinforcing the hypothesis that Mn Ox/Hx precipitated in relation to meteoric diagenesis of the Santanyí Limestone during subaerial exposure after its deposition.

The origin and source for the Mn Ox/Hx remain uncertain and will need further studies. Precipitation of Mn Ox/Hx has been extensively documented in soil profiles and desert varnish, commonly related to microbial activity (e.g. Dorn & Oberlander, 1981; Jones, 1991; Maynard, 2003; Garvie *et al.*, 2008; Northup *et al.*, 2010; Eren *et al.*, 2014; Xu *et al.*, 2018; 2019, and references therein). Manganese geochemistry in sedimentary environments is governed by

oxidation and reduction processes, as well as by biotic processes (Maynard, 2003, and references therein). According to this author, at pH values of 5 to 7 for freshwaters, Mn should be soluble except under strongly oxidizing conditions and, in soil profiles, the high mobility of Mn may produce significant Mn enrichment downward. Moreover, this author points out that the presence of organic matter in sediments or aquifers allows the release of soluble Mn into the overlying water or into the down-flow part of the aquifer and that the slow abiotic precipitation rates of manganese oxides also provide an opportunity for bacterial mediation in oxidation. In that regard, Zhang *et al.* (2002) observed in an experimental study, that at circumneutral pH, the rate of biologically mediated Mn^{2+} oxidation likely exceeds abiotic Mn^{2+} oxidation at relatively low concentrations of Mn oxidizing bacteria.

Regarding the source of Mn, several authors have proposed that the components of the rock varnish are externally derived and are transported via aeolian activity (Jones, 1991, and references therein). This author performed an experimental study in coastal soil samples in contact with water–CO_2 solutions and proposed that natural fogs or dews release Mn when they come in contact with aeolian materials on rock surfaces and that this mechanism may efficiently provide Mn to bacteria on varnishing surfaces. Several authors have subsequently interpreted that Mn in varnish surfaces are derived from leaching of dust particles during wetting by dew, fog droplets and rain (e.g. Thiagarajan & Aeolus Lee, 2004; Goldsmith *et al.*, 2014; Xu *et al.*, 2019). In this regard, Huang *et al.* (2008) noticed that the contents of MnO_2, Fe_2O_3 and CaO in cutans of subtropical soils of China were higher than those in matrix soils and interpreted that these cutans grew in environments of alternating wet and dry conditions, in which, when soil became dry, the dissolved Mn^{2+} was oxidized and deposited on cracks or surfaces of the soil.

Thus, following all of these works, Mn in the studied area could have been transported in dust particles by the winds, and, after leaching, Mn Ox/Hx would have precipitated during the subaerial exposure of the Santanyí Limestone, associated with the Messinian crisis (Fig. 1C; Arenas & Pomar, 2010). Precipitation was linked to the input of relatively acidic freshwaters and under oxidizing conditions, undergoing periods of wetting and drying and, probably, also linked to biotic processes. Manganese could move downward, due to its high mobility under typical freshwater pH, and Mn Ox/Hx could precipitate mainly in the most porous and permeable grainy facies of Bed 2. The fact that most Mn Ox/Hx precipitated in the microbialite-rich Bed 2 also suggests that the high content in organic matter played a role in their precipitation. Nevertheless,

to fully understand the Mn Ox/Hx origin and precipitation, further and more detailed study is being carried out.

CONCLUSIONS

A new outcrop of the uppermost Santanyí Limestone (in Southern Mallorca, Spain), here described for the first time, indicates deposition in a restricted, grain-dominated and burrowed shallow-water platform. A laterally extensive microbialite biostrome marks a shift from those conditions to deposition dominated by benthic microbial communities, with a multi-storey accretion significantly influenced by bioturbation.

The most outstanding features of the biostrome are its dark colour and columnar structure. The dark colour is caused by post-depositional precipitation of manganese oxyhydroxides during meteoric diagenesis linked to subaerial exposure of the Santanyí Limestone, and probably influenced by biotic processes. These Mn minerals have a complex and intriguing diagenetic history that deserves further study.

The columnar structure of the biostrome includes some features consistent with an accretionary origin of the columns, but others point to a likely role of metazoan bioturbation during, or very soon after, microbial accretion and lithification. Thus, the columnar structure of the studied example is interpreted as due to microbial accretion coeval with metazoan disruption and filling of the intercolumnar space by grainy sediment, including faecal products of the bioturbating organisms, such as crustaceans. Bioturbation is scarcely described within microbialites and, when it is, it often has a destructive role. Here, a model is presented in which concurrent accretion and bioturbation are the keys to the morphogenesis of columnar microbialites. Further research on other Phanerozoic and Late Proterozoic examples will test whether this model is an oddity or a common interaction between metazoans and benthic microbial communities.

ACKNOWLEDGEMENTS

Funded by projects CGL2013-42867-P, CGL2014-52096-P, CGL2014-52670-P and CGL2018-094034-B-C21 (Spanish Government) and E32_17R (European Funds of Regional Development, Aragón Government, Operating Program FEDER Aragón 2014-2020), and by the 'Sedimentary geology, palaeoclimate and environmental change' Research Group of the Complutense University of Madrid–Madrid Community. We are thankful to Beatriz Moral, Aitor Antón, Juan Carlos Salamanca, Joaquín Perona and Rodolfo Pozuelo, for technical support. We thank the personnel of the *Servicio General de Apoyo a la Investigación* of the University of

Zaragoza, and the *Serveis Cientificotécnics* of the University of Barcelona. The authors would like to thank Carlos Cónsole-Gonella and an anonymous reviewer for their constructive suggestions and comments.

DATA AVAILABILITY STATEMENT

The data that support the findings of this study are available in the text and figures of this manuscript.

REFERENCES

Abreu, V.S. and **Haddad, G.A.** (1998) Glacioeustatic fluctuations: the mechanism linking stable isotope events and sequence stratigraphy from the Early Oligocene to Middle Miocene. In: *Mesozoic and Cenozoic Sequence Stratigraphy of European Basins* (Eds P.C. de Graciansky, J. Hardenbol, T. Jacquin and P.R.Vail) *SPEM Spec. Publ.*, **60**, p. 245-259.

Aitken, J.D. (1967) Classification and environmental significance of cryptalgal limestones and dolomites, with illustrations from the Cambrian and Ordovician of southwestern Alberta. *J Sed. Petrol.*, **37**, 1163-1178.

Akpan, E.B. (1991) Palaeoecological significance of *Lithophaga* borings in Albian stromatolites, SE Nigeria. *Palaeogeogr. Palaeocl. Palaeoecol.*, **88**, 185-192.

Andres, M.S. and **Reid, R.P.** (2006) Growth morphologies of modern marine stromatolites: A case study from Highborne Cay, Bahamas. *Sed. Geol.*, **185**, 319-328.

Arenas, C. and **Pomar, L.** (2010) Microbial deposits in upper Miocene carbonates, Mallorca, Spain. *Palaeogeogr. Palaeocl. Palaeoecol.*, **297**, 465-485.

Arenas, C., Cabrera, L. and **Ramos, E.** (2007) Sedimentology of tufa facies and continental microbialites from the Palaeogene of Mallorca Island (Spain). *Sed. Geol.*, **197**, 1-27.

Arp, G., Hofmann, J. and **Reitner, J.** (1998) Microbial fabric formation in spring mounds ("microbialites") of alkaline salt lakes in the Badain Jaran Sand Sea, PR China. *Palaios*, **13**, 581-592.

Awramik, S.M. (1991) Precambrian columnar stromatolite diversity: Reflection of metazoan appearance. *Science*, **174**, 825-827.

Awramik, S.M. and **Sprinkle, J.** (1999) Proterozoic stromatolites: The first marine evolutionary biota. *Historical Biology*, **13**, 241-253.

Batchelor, M.T., Burne, R.V., Henry, B.I. and **Watt, S.D.** (2003) Mathematical and image analysis of stromatolite morphogenesis. *Math. Geol.*, **35**, 789-803.

Bathurst, R.G.C. (1975) Carbonate sediments and their diagenesis. Elsevier, Amsterdam, 658 pp.

Bertrand-Sarfati, J. (1972) Paléoécologie de certains stromatolites en récifs des formations du Précambrien Supérieur du Groupe d'Atar (Mauritanie Sahara Occidental): Création d'espèces nouvelles. *Palaeogeog., Palaeoclimatol. Palaeoecol.*, **11**, 33-63.

Bertrand-Sarfati, J., Freytet, P. and **Plaziat, J.C.** (1994) Microstructures in Tertiary nonmarine stromatolites (France). Comparison with Proterozoic. In: *Phanerozoic Stromatolites II* (Eds J. Bertrand-Sarfati and C. Monty) Kluwer Academic Publishers, Dordrecht, pp. 155-191.

Blumenberg, M., Thiel, V. and **Reitner, J.** (2015) Organic matter preservation in the carbonate matrix of a recent microbial mat – Is there a 'mat seal effect'? *Organic Geochem.*, **87**, 25-34.

Bosak, T., Knoll, A.H. and **Petroff, A.P.** (2013) The meaning of stromatolites. *Ann. Rev. Earth Planet. Sci.,* **41**, 21-44.

Bourillot, R., Vennin, E., Dupraz, C., Pace, A., Foubert, A., Rouchy, J.M., Patrier, P., Blanck, Ph., Bernard, D., Lesseur, J. and **Visscher, P.T.** (2020) The Record of Environmental and Microbial Signatures in Ancient Microbialites: The Terminal Carbonate Complex from the Neogene Basins of Southeastern Spain. *Minerals*, **10**, 276.

Brook, G.A., Railsback, L.B. and **Marais, E.** (2011) Reassessment of carbonate ages by dating both carbonate and organic material from an Etosha Pan (Namibia) stromatolite: Evidence of humid phases during the last 20 ka. *Quatern. Int.*, **229**, 24-37.

Buatois, L.A. and **Mángano, G.** (2013) Ichnology: Organism–substrate interactions in space and time. Cambridge University Press, Cambridge, 347 pp.

Burne, R.V. and **Moore, L.S.** (1987) Microbialites: Organosedimentary deposits of benthic microbial communities. *Palaios*, **2**, 241-254.

Campos-Soto, S., Cobos, A., Caus, E., Benito, M.I., Fernández-Labrador, L., Suarez-Gonzalez, P., Quijada, I.E., Mas, R., Royo-Torres, R. and **Alcalá, L.** (2017) Jurassic Coastal Park: A great diversity of palaeoenvironments for the dinosaurs of the Villar del Arzobispo Formation (Teruel, eastern Spain). *Palaeogeogr., Palaeoclimatol., Palaeoecol.*, **485**, 154-177.

Campos-Soto, S., Benito, M.I., Cobos, A., Caus, E., Quijada, I.E., Suarez-Gonzalez, P., Mas, R., Royo-Torres, R. and **Alcalá, L.** (2019) Revisiting the age and palaeoenvironments of the Upper Jurassic–Lower Cretaceous? dinosaur-bearing sedimentary record of eastern Spain: implications for Iberian palaeogeography. *J. Iberian Geol.*, **45**, 471-510.

Chafetz, H.S. and **Buczynski, C.** (1992) Bacterially induced lithification of microbial mats. *Palaios*, **7**, 277-293.

Chagas, A.A.P., Webb, G.E., Burne, R.V. and **Southam, G.** (2016) Modern lacustrine microbialites: Towards a synthesis of aqueous and carbonate geochemistry and mineralogy. *Earth-*

Sci. Rev., **162**, 338-363.**Choquette, P.W.** and **Pray L.C.** (1970) Geologic nomenclature and classification of porosity in sedimentary carbonates. *Bull. Am. Ass. Petrol. Geol.*, **54**, 207-250.

Cónsole-Gonella, C.A. and **Marquillas, R.A.** (2014) Bioclaustration trace fossils in epeiric shallow marine stromatolites: the Cretaceous-Palaeogene Yacoraite Formation, Northwestern Argentina. *Lethaia*, **47**, 107-119.

Cónsole-Gonella, C.A., Griffin, M. and **Aceñolaza, F.G.** (2009) Gastropods associated with fossil traces from Yacoraite Formation (Maastrichtian-Danian), and its paleoenvironmental significance, Jujuy, Northwestern Argentina. *Acta Geol. Sinica*, **83**, 860-867.

Cao, R.J. (1988) Study on stromatolitic decline event in terminal Precambrian. *Acta Palaeont. Sinica*, **27**, 737-750.

Demicco, R.V. and **Hardie, L.A.** (1994) Sedimentary structures and early diagenetic features of shallow marine carbonate deposits. *SEPM Atlas Series*, 1, 265 pp.

Dickson, J.A.D. (1966) Carbonate identification and genesis as revealed by staining. *J. Sed. Petrol.*, **36**, 491-505.

Dondi, L. and **Papetti, I.** (1966) Segnalazione di copropliti nel Miocene dell'Italia meridionale. *Geol. Romana*, **5**, 55-68.

Dorn, R.L. and **Oberlander, T.M.** (1981) Microbial origin of desert varnish. *Science*, **213**, 1245-1247.

Druschke, P.A., Jiang, G., Anderson, T.B. and **Hanson, A.D.** (2009) Stromatolites in the Late Ordovician Eureka Quartzite: implications for microbial growth and preservation in siliciclastic settings. *Sedimentology*, **56**, 1275-1291.

Drysdale, R.N. (1999) The sedimentological significance of hydropsychid caddis-fly larvae (order: Trichoptera) in a travertine-depositing stream: Louie Creek, Northwest Queensland, Australia. *J. Sed. Res.*, **69**, 145-150.

Dunham, R.J. (1962) Classification of carbonate rocks according to depositional texture. In: *Classification of Carbonate Rocks* (Ed. W.E. Ham). AAPG Memoir, 1, pp. 108-121.

Dupraz, C., Visscher, P.T., Baumgartner, L.K. and **Reid, R.P.** (2004) Microbe–mineral interactions: early carbonate precipitation in a hypersaline lake (Eleuthera Island, Bahamas). *Sedimentology*, **51**, 745-765.

Dupraz, C., Pattisina, R. and **Verrecchia, E.R.** (2006) Translation of energy into morphology: simulation of stromatolite morphospace using a stochastic model. *Sediment. Geol.*, **185**, 185-203.

Ekdale, A.A., Brown, F.H. and **Feibel, C.S.** (1989) Nonmarine macroborings in Early Pleistocene algal biolithites (stromatolites) of the Turkana Basin, northern Kenya. *Palaios*, **4**, 389-396.

Eren, M., Kadir, S., Zucca, C., Akşit, I., Kaya, Z. and **Kapur, S.** (2014) Pedogenic manganese oxide coatings (calcium buserite) on fracture surfaces in Tortonian (Upper Miocene) red mudstones, southern Turkey. *Catena*, **116**, 149-156.

Ezaki, Y., Liu, J., Adachi, N. and **Yan, Z.** (2017) Microbialite development during the protracted inhibition of skeletal-dominated reefs in the Zhangxia Formation (Cambrian Series 3) in Shandong Province, North China. *Palaios*, **32**, 559-571.

Farmer, J.D. (1992) Grazing and bioturbation in modern microbial mats. In: *The Proterozoic Biosphere* (Eds J.W. Schopf and C. Klein), pp. 295-297, Cambridge University Press, Cambridge.

Flügel, E. (2010) Microfacies of Carbonate Rocks. Springer, Berlin, 984 pp.

Föllmi, K.B., Delamette, M. and **Ouwehand, P.J.** (2011) Aptian to Cenomanian deeper-water hiatal stromatolites from the northern Tethyan margin. In: *Stromatolites: Interaction of microbes with sediments* (Eds V.C. Tewari and J. Sekbach) pp. 159-186. Springer, Berlin.

Fornós, J.J. and **Pomar, L.** (1983) Mioceno superior de Mallorca: Unidad calizas de Santanyí ("Complejo terminal"). In: *El Terciario de las Baleares (Mallorca - Menorca)* (Eds L. Pomar, J. Obrador, J. Fornós, and A. Rodríguez-Perea) *Guía de las excursiones X Congreso Nacional de Sedimentología*, 177-206.

García-Pichel, F., Al-Horani, F.A., Farmer, J.D., Ludwig, R. and **Wade, B.D.** (2004) Balance between microbial calcification and metazoan bioerosion in modern stromatolitic oncolites. *Geobiology*, **2**, 49-57.

Garrett, P. (1970) Phanerozoic stromatolites: Noncompetitive ecologic restriction by grazing and burrowing animals. *Science*, **169**, 171-173.

Garvie, L.A.J., Burt, D.M. and **Buseck, P.R.** (2008) Nanometer-scale complexity, growth, and diagenesis in desert varnish. *Geology*, **36**, 215-218.

Glumac, B. and **Wlaker, K.R.** (1997) Selective dolomitization of Cambrian microbial carbonate deposits: a key to mecahnisms and environments of origin. *Palaios*, **12**, 98-110.

Goldsmith, Y., Stein, M. and **Enzel, Y.** (2014) From dust to varnish: geochemical constraints on rock varnish formation in the Negev Desert, Israel. *Geochim. Cosmochim. Acta*, **126**, 97-111.

Golubic, S. (1976) Organisms that Build Stromatolites. In: *Stromatolites* (Ed. W.R. Walter) *Dev. Sedimentol.*, **20**, pp. 113-126.

Gradziński, M. (2010) Factors controlling growth of modern tufa: results of a field experiment. In: Tufas and Speleothems: Unravelling the Microbial and Physical Controls (Eds M. Pedley and M. Rogerson), Geol. Soc. Spec. Publ., 336, 143–191.

Grey, K. and **Awramik, S.M.** (2020) Handbook for the study and description of microbialites. *Bull. Geol. Surv. W. Aust.*, **147**, 278 pp.

Grotzinger, J.P. (1990) Geochemical model for Proterozoic stromatolite decline. *Am. J. Sci.*, **290-A**, 80-103.

Grotzinger, J.P. and **Knoll, A.H.** (1999) Stromatolites in Precambrian carbonates: Evolutionary mileposts or environmental dipsticks? *Annu. Rev. Earth Planet. Sci.*, **27**, 313-358.

Grotzinger, J.P. and **Rothman, D.H.** (1996) An abiotic model for stromatolite morphogenesis. *Nature*, 383, 423-425.

Harwood Theisen, C. and **Sumner, D.Y.** (2016) Thrombolite fabrics and origins: Influences of diverse microbial and metazoan processes on Cambrian thrombolite variability in the Great Basin, California and Nevada. *Sedimentology*, **63**, 2217-2252.

Hasiotis, S.T. (2004) Reconnaissance of Upper Jurassic Morrison Formation ichnofossils, Rocky Mountain Region, USA: paleoenvironmental, stratigraphic, and paleoclimatic significance of terrestrial and freshwater ichnocoenoses. *Sed. Geol.*, **167**, 177-268.

Ibarra, Y., Corsetti, F.A., Greene, S.E. and **Bottjer, D.J.** (2014) Microfacies of the cotham Marble: A tubestone carbonate microbialite from the Upper Triassic, Southwestern U.K. *Palaios*, **29**, 1-15.

Hägele, D., Leinfelder, R., Grau, J., Burmeister, E.-G. and **Struck, U.** (2006) Oncoids from the river Alz (southern Germany): tiny ecosystems in a phosphorus-limited environment. *Palaeogeogr. Palaeoclimatolol. Palaeoecol.*, **237**, 378–395.

Hickman-Lewis, K., Gautret, P., Arbaret, L., Sorieul, S., De Wit, R., Foucher, F., Cavalazzi, B. and **Westall, F.** (2019) Mechanistic Morphogenesis of Organo-Sedimentary Structures Growing Under Geochemically Stressed Conditions: Keystone to Proving the Biogenicity of Some Archaean Stromatolites? *Geosciences*, **9**, 359.

Hoffman, P. (1976a) Environmental diversity of Middle Precambrian stromatolites. In: *Stromatolites* (Ed. M.R. Walter) *Dev. Sedimentol.*, **20**, pp. 599-611.

Hoffman, P. (1976b) Stromatolite morphogenesis in Shark Bay, Western Australia. In: *Stromatolites* (Ed. M.R. Walter) *Dev. Sedimentol.*, **20**, pp. 261-271.

Hofmann. H.J. (1969) Attributes of stromatolites. *Geol. Surv. Can. Pap.*, **69-39**, 58 pp.

Huang, L., Hong, J., Tan, W.F., Hu, H.Q., Liu, F. and **Wang, M.K.** (2008) Characteristics of micromorphology and element distribution of iron-manganese cutans in typical soils of subtropical China. *Geoderma*, **146**, 40-47.

Jahnert, R.J. and **Collins, J.B.** (2011) Significance of subtidal microbial deposits in Shark Bay, Australia. *Mar. Geol.*, **286**, 106-111.

Jahnert, R.J. and **Collins, J.B.** (2013) Controls on microbial activity and tidal flat evolution in Shark Bay, Western Australia. *Sedimentology*, **60**, 1071-1099.

James, N.P. and Choquette, P.W. (1990) Limestones - The meteoric diagenetic environment. In: *Diagenesis* (Eds. I.A. McIlreath, D.W. Morrow) pp. 35-73. Geoscience Canada, Reprint Series 4.

Jones, C.E. (1991) Characteristics and origin of rock varnish from the hyperarid coastal deserts of northern Peru. *Quatern. Res.*, **35**, 116-129.

Kennard, J.M. (1994) Thrombolites and stromatolites within shale-carbonate cycles, Middle-Late Cambrian Shannon Formation, Amadeus Basin, Central Australia. In: *Phanerozoic Stromatolites II* (Eds J. Bertrand-Sarfati and C. Monty), pp. 443-471, Kluwer Academic Publishers, Dordrecht.

Kennard, J.M. and **James, N.P.** (1986) Thrombolites and stromatolites: two distinct types of microbial structures. *Palaios*, **1**, 492-503.

Kennedy, W.J. (1975) Trace fossils in carbonate rocks. In: *The Study of Trace Fossils* (Ed. R.W. Frey) pp. 377-398, Springer, Berlin.

Kennedy, W.J., Jakobson, M.E. and **Johnson, R.T.** (1969) A *Favreina-Thalassinoides* association from the Great Oolite of Oxfordshire. *Palaeontology*, **12**, 549-554.

Knaust, D. (2020) Invertebrate coprolites and cololites revised. *Pap. Palaeontol.*, https://doi.org/10.1002/spp2.1297

Knaust, D., Curran, H.A. and **Dronov, A.V.** (2012) Shallow-marine carbonates. In: *Trace Fossils as Indicators of Sedimentary Environments* (Eds D. Knaust and R.G. Bromley) pp. 705-750, Elsevier, Amsterdam.

Lamond, R.E. and **Tapanila, L.** (2003) Embedment Cavities in Lacustrine Stromatolites: Evidence of Animal Interactions from Cenozoic Carbonates in U.S.A. and Kenya. *Palaios*, **18**, 445-453.

Machel, H.G. and **Burton, E.** (1991) Factors Governing Cathodoluminescence in Calcite and Dolomite and their Implications for Studies of Carbonate Diagenesis. In: *Luminescence*

microscopy and Spectroscopy: Qualitative and Quantitative Applications (Eds Ch.E. Barker and O.C. Kopp), *SEPM Short Course*, 25, 37-58.

Mas, G. and **Fornós, J.J.** (2006) Aportacions al coneixement del Neogen postorogènic de la cubeta sedimentària de Campos (Mallorca, Illes Balears, Mediterrània occidental). *Boll. Soc. Hist. Nat. Balears*, **49**, 67-81.

Mas, G. (2015) El registre estratigràfic del Messinià terminal i del Pliocè a l'illa de Mallorca. Relacions amb la crisi de salinitat de la Mediterrània. PhD Thesis. Universitat de les Illes Balears, 534 pp. Available in: https://www.tdx.cat/handle/10803/375904

Massari, F. and **Westphal, H.** (2011) Microbialites in the Middle–Upper Jurassic Ammonitico Rosso of the Southern Alps (Italy). In: *Stromatolites: Interaction of microbes with sediments* (Eds V.C. Tewari and J. Sekbach) pp. 223-250. Springer, Berlin.

Martin-Bello, L., Arenas, C. and **Jones, B.** (2019) Lacustrine stromatolites: useful structures for environmental interpretation. An example from the Miocene Ebro Basin. *Sedimentology*, **66**, 2098-2133.

Maynard, J.B. (2003) Manganiferous sediments, rocks and ores. In: *Treatise on Geochemistry* (Eds K.K. Turekian, and H.D. Holland), pp. 289-308, Elsevier, Amsterdam.

Monty, C.L.V. (1973) Precambrian background and Phanerozoic history of stromatolitic communities, an overview. *Ann. Soc. Géol. Belg.*, **96**, 585-624.

Monty, C.L.V. (1976) The origin and development of cryptalgal fabrics. In: *Stromatolites* (Ed. M.R. Walter) *Dev. Sedimentol.*, **20**, pp. 193-249.

Northup, D.E., Snider, J.R., Spilde, M.N., Porter, M.L., van de Kamp, J.L., Boston, P.J., Nyberg, A.M. and **Bargar, J.R.** (2010) Diversity of rock varnish bacterial communities from Black Canyon, New Mexico. *J. Geophys. Res*, **115**, G02007.

Pierre, C. and **Rouchy, J.M.** (1988) Carbonate replacements after sulfate evaporites in the middle Miocene of Egypt. *J. of Sed. Petrol.*, **58**, 446-456.

Planavsky, N. and **Ginsburg, R.N.** (2009) Taphonomy of modern marine Bahamian microbialites. *Palaios*, **24**, 5-17.

Pomar, L. and **Ward, W.C.** (1994) Response of a Miocene carbonate platform to high frequency eustasy. *Geology*, **22**, 131-134.

Pomar, L., Marzo, M. and **Barón, A.** (1983) El Terciario de Mallorca. In: *El Terciario de las Baleares (Mallorca - Menorca). Guía de las excursiones.* (Eds L. Pomar, J. Obrador, J. Fornós, and A. Rodríguez-Perea). X Congreso Nacional de Sedimentología, Menorca, pp 21-44.

Pomar, L., Ward, W.C. and **Green, D.G.** (1996) Upper Miocene reef complex of the Llucmajor Area, Mallorca, Spain. In: *Models for Carbonate Stratigraphy from Miocene Reef Complexes of Mediterranean Regions* (Eds E.K Franseen, M. Esteban, W.C. Ward and J.M. Rouchy) *SEPM Concepts in Sedimentology and Paleontology*, **5**, pp. 191-225.

Pratt, B.R. (1982) Stromatolite decline – A reconsideration. *Geology*, **10**, 512-515.

Purdy, E.G. (1963a) Recent Calcium Carbonate Facies of the Great Bahama Bank. 1. Petrography and Reaction Groups. *J. Geol.*, **71**, 334-355.

Purdy, E.G. (1963a) Recent Calcium Carbonate Facies of the Great Bahama Bank. 2. Sedimentary Facies. *J. Geol.*, **71**, 472-497.

Quijada, I.E. (2014) Evolución sedimentaria y paleogeografía de los sistemas costeros siliciclásticos y carbonático-evaporíticos del Grupo Oncala (Berriasiense, Cuenca de Cameros Oriental). PhD Thesis available online at: https://eprints.ucm.es/28967/1/T35885.pdf, 316 pp.

Quijada, I.E.; Suarez-Gonzalez, P.; Benito, M.I. and **Mas, R.** (2013) Depositional depth of laminated carbonate deposits: Insights from the Lower Cretaceous Valdeprado Fromation (Cameros Basin, Northern Spain). *J. Sedim. Research*, **83**, 241-257.

Quijada, I.E.; Suarez-Gonzalez, P.; Benito, M.I.; Lugli, S. and **Mas, R.** (2014) From carbonate-sulphate interbeds to carbonate breccias: The role of tectonic deformation and diagenetic processes (Cameros Basin, Lower Cretaceous, N Spain). *Sed. Geol.*, **312**, 76-93.

Quijada, I.E.; Benito, M.I.; Suarez-Gonzalez, P.; Rodríguez-Martínez, M.; and **Campos-Soto, S.** (2020) Challenges to carbonate-evaporite peritidal facies models and cycles: insights from Lower Cretaceous stromatolite-bearing deposits (Oncala Group, N Spain). *Sed. Geol.*, 105752, https://doi.org/10.1016/j.sedgeo.2020.105752

Raaben, M.E. (2006) Dimensional parameters of columnar stromatolites as a result of stromatolite ecosystem evolution. *Strat. Geol. Correl.*, **14**, 150-163.

Radke, B.M. (1980) Epeiric carbonate sedimentation of the Ninmaroo Formation (Upper Cambrian-Lower Ordovician), Georgina Basin. *BMR J. Australian Geol. Geophys.*, **5**, 183-200.

Reid, R.P., Foster, J.S., Radtke, G. and **Golubic, S.** (2011) Modern marine stromatolites of Little Darby Island, Exuma Archipelago, Bahamas: Environmental setting, accretion mechanisms and role of euendoliths. In: Advances in Stromatolite Geobiology (Eds J. Reitner, N.V. Quéric and G. Arp) *Lect. Notes Earth Sci.*, **131**, pp. 77-89.

Reijmer, J.J.G., Swart, P.K., Bauch, T., Otto, R., Reuning, L., Roth, S. and **Zechel, S.** (2009) A re-evaluation of facies on Great Bahama Bank I: new facies maps of western Great

Bahama Bank. In: Perspectives in Carbonate Geology (Eds P.K. Swart, G.P. Eberli and J.A. McKenzie) *IAS Spec. Publ.*, **41**, pp. 29-46.

Reitner, J. (1993) Modern cryptic microbialite/Metazoan facies from Lizard Island (Great Barrier Reef, Australia). Formation and concepts. *Facies*, **29**, 3-40.

Reitner, J., Quéric, N-V. and **Reich, M.** (eds.) (2011). Advances in Stromatolite Geobiology. Lecture Notes in Earth Sciences 131, Springer-Verlag, Berlin Heidelberg, 560.

Riding, R. (1999) The term stromatolite: towards an essential definition. *Lethaia*, **32**, 321-330.

Riding, R. (2006) Microbial carbonate abundance compared with fluctuations in metazoan diversity over geological time. *Sed. Geol.*, **185**, 229-238.

Riding, R. (2011) Microbialites, stromatolites, and thrombolites. In: *Encyclopedia of Geobiology* (Eds J. Reitner and V. Thiel), pp. 635-654, Springer, Berlin.

Riding, R. and **Tomás, S.** (2006) Stromatolite reef crusts, Early Cretaceous, Spain: bacterial origin of in situ-precipitated peloid microspar? *Sedimentology*, **53**, 23-34.

Riding, R., Awramik, S.M., Winsborough, B.M., Griffin, K.M. and **Dill, R.F.** (1991) Bahamian giant stromatolites: microbial composition of surface mats. *Geol. Mag.*, **128**, 227-234.

Rishworth, G.M., Perissinotto, R. and **Bird, M.S.** (2016) Coexisting living stromatolites and infaunal metazoans. *Oecologia*, **182**, 539-545.

Rishworth, G.M., Edwards, M.J.K., Cónsole-Gonella, C. and **Perissinotto, R**. (2019) Modern active microbialite-metazoan relationships in peritidal systems on the Eastern Cape coast of South Africa: Ecological significance and implication for the palaeontological record. *J. Afr. Earth Sci.*, **153**, 1-8.

Rodríguez-Martínez, M. (2011) Mud Mounds. In: *Encyclopedia of Geobiology* (Eds J. Reitner and V. Thiel), pp. 667-675, Springer, Berlin.

Rodríguez-Martínez, M. and **Reitner, J.** (2015) Paleoenvironmental reconstruction of a downslope accretion history: From coralgal-coralline sponge rubble to mud mound deposits (Eocene, Ainsa Basin, Spain). *Sed. Geol.*, **330**, 16-31.

Rodríguez-Martínez, M., Sánchez, F., Walliser, E.O. and **Reitner, J.** (2012) An Upper Turonian fine-grained shallow marine stromatolite bed from the Muñecas Formation, Northern Iberian Ranges, Spain. *Sed. Geol.*, **263-264**, 96-108.

Schirrmeister, B.E., Sanchez-Baracaldo, P. and **Wacey, D.** (2016). Cyanobacterial evolution during the Precambrian. *Int. J. Astrobiology*, **15** (3), 187–204.

Scholle, P.A. and **Ulmer-Scholle** (2003) A color guide to the petrography of carbonate rocks: Grains, textures, porosity, diagenesis. AAPG Memoir 77. The American Association of Petroleum Geologists, Tulsa, 459 pp.

Schweigert, G., Seegis, D.B., Fels, A. and **Leinfelder, R.R.** (1997) New internally structured decapod microcoprolites from Germany (Late Triassic/Early Miocene), Southern Spain (Early/Middle Jurassic) and Portugal (Late Jurassic): Taxonomy, palaeoecology and evolutionary implications. *Paläontol. Z.*, **71**, 51-69.

Sellwood, B.W. (1971) A *Thalassinoides* burrow containing the crustacean *Glyphaea udressieri* (Meyer) from the Bathonian of Oxfordshire. *Palaeontology*, **14**, 589-591.

Semikhatov, M.A., Gebelein, C.D., Cloud, P., Awramik, S.M. and **Benmore, W.C.** (1979) Stromatolite morphogenesis—progress and problems. *Can. J. Earth Sci.*, **16**, 992-1015.

Serebryakov, S.N. (1976) Biotic and abiotic factors controlling the morphology of Riphean stromatolites. In: *Stromatolites* (Ed. M.R. Walter) *Dev. Sedimentol.*, **20**, pp. 321-336.

Shapiro, R.S. (2000) A comment on the systematic confusion of thrombolites. *Palaios*, **15**, 166-169.

Shen, J.W. and **Webb, G.E.** (2005) Metazoan–microbial framework fabrics in a Mississippian (Carboniferous) coral–sponge–microbial reef, Monto, Queensland, Australia. *Sed. Geol.*, **178**, 113-133.

Shen, Y., Thiel, V., Duda, J.P. and **Reitner, J.** (2018) Tracing the fate of steroids through a hypersaline microbial mat (Kiritimati, Kiribati/Central Pacific). *Geobiology*, **16**, 307-318.

Shen, Y., Thiel, V., Suarez-Gonzalez, P., Rampen, S.W. and **Reitner, J.** (2020) Sterol preservation in hypersaline microbial mats. *Biogeosciences*, **17**, 649-666.

Sprechmann, P., Gaucher, C., Blanco, G. and **Montaña, J.** (2004) Stromatolitic and trace fossils community of the Cerro Victoria Formation, Arroyo del Soldado Group (Lowermost Cambrian, Uruguay). *Gondwana Res.*, **7**, 753-766.

Suarez-Gonzalez, P., Arenas, C., Benito, M.I. and **Pomar, L.** (2019a) Interplay between biotic and environmental conditions in pre-salt Messinian microbialites of the western Mediterranean (Upper Miocene, Mallorca, Spain). *Palaeogeog. Palaeocl. Palaeoecol.*, **533**, 109242

Suarez-Gonzalez, P., Benito, M.I., Quijada, I.E., Mas, R. and **Campos-Soto, S.** (2019b) 'Trapping and binding': A review of the factors controlling the development of fossil agglutinated microbialites and their distribution in space and time. *Earth-Sci. Rev.*, **194**, 182-215.

Suarez-Gonzalez, P., Quijada, I.E., Benito, M.I., Campos-Soto, S. and **Rodríguez-Martínez, M.** (2019c) Interaction of constructive and destructive processes in peritidal stromatolites: build-up, tear-down, eat-up and re-build. *16th Bathurst Meeting. Mallorca, July 2019. Abstracts Volume*, P-178. Available in: https://www.mallorca-bathurst-2019.com/

Suosaari, E.P., Awramik, S.M., Reid, R.P., Stolz, J.F. and **Grey, K.** (2018) Living dendrolitic microbial mats in Hamelin Pool, Shark Bay, Western Australia. *Geosciences*, **8**, 212. doi:10.3390/geosciences8060212

Tarhan, L.G., Planavsky, N.J., Laumer, C.E., Stolz, J.F. and **Reid, R.P.** (2013) Microbial mat controls on infaunal abundance and diversity in modern marine microbialites. *Geobiology*, **11**, 485-497.

Thiagarajan, N. and **Aeolus Lee C.T.** (2004) Trace-element evidence for the origin of desert varnish by direct aqueous atmospheric deposition. *Earth Planet. Sci. Lett.*, **224**, 131-141.

Tomás, S., Homann, M., Mutti, M., Amour, F., Christ, N., Immenhauser, A., Agar, S.M. and **Kabiri, L.** (2013) Alternation of microbial mounds and ooid shoals (Middle Jurasssic, Morocco): Response to paleoenvironmental changes. *Sed. Geol.*, **294**, 68-82.

Tosti, F. and **Riding, R.** (2017) Current molded, storm damaged, sinuous columnar stromatolites: Mesoproterozoic of northern China. *Palaeogeogr. Palaeocl. Palaeoecol.*, **465**, 93-102.

Tucker, M. and **Wright, V.P.** (1990) Carbonate sedimentology. Blackwell, Oxford, 482 pp.

Vanyo, J.P. and **Awramik, S.M.** (1985) Stromatolites and Earth—Sun—Moon dynamics. *Precambrian Res.*, **29**, 121-142.

Vennin, E., Olivier, N., Brayard, A., Bour, I., Thomazo, C., Escarguel, G., Fara, E., Bylund, K.G., Jenks, J.F., Stephen, D.A. and **Hofmann, R.** (2015) Microbial deposits in the aftermath of the end-Permian mass extinction: A diverging case from the Mineral Mountains (Utah, USA). *Sedimentology*, **62**, 753-792.

Walter, M.R. (1972) Stromatolites and the biostratigraphy of the Australian Precambrian and Cambrian. Special Paper in Paleontology 11, 190 pp.

Walter, M.R. (1976) Appendix I: Glossary of selected terms. In: *Stromatolites* (Ed. M.R. Walter) *Dev. Sedimentol.*, **20**, pp. 687-692.

Walter, M.R., Bauld, J. and **Brock, T.D.** (1976) Microbiology and morphogenesis of columnar stromatolites (*Conophyton*, *Vacerrilla*) from hot springs in Yellowstone National Park. In: *Stromatolites* (Ed. M.R. Walter) *Dev. Sedimentol.*, **20**, pp. 273-310.

Walter, M.R. and **Heys, G.R.** (1985) Links between the rise of the Metazoa and the decline of stromatolites. *Precambrian Res.*, **29**, 149-174.

Warren, J.K. (2016) Evaporites. A Geological Compendium. 2nd Edition. Springer, Heidelberg, 1813 pp.

Wright, V.P. and **Mayall, M.** (1981) Organism-sediment interactions in stromatolites: and example from the Upper Triassic of South West Britain. In: *Phanerozoic Stromatolites* (Ed. C. Monty), pp.74-84, Springer, Berlin.

Xu, X., Ding, H., Li, Y., Lu, A., Li, Y. and **Wang, C.** (2018) Mineralogical characteristics of Mn coatings from different weathering environments in China: clues on their formation. *Mineral. Petrol.*, **112**, 671-683.

Xu, X., Li, Y., Li, Y., Lu, A., Qiao, R., Liu, K., Ding, H. and **Wang, C.** (2019) Characteristics of desert varnish from nanometer to micrometer scale: A photo-oxidation model on its formation. *Chem. Geol.*, **522**, 55-70.

Zhang. J., Lion, L.W., Nelson, Y.M., Shuler, M.L and **Ghiorse, W.C. (2002)** Kinetics of Mn(II) oxidation by *Leptothrix discophora* SS1. *Geochim. Cosmochim. Acta*, **65**, 773-781.

FIGURE CAPTIONS

Fig. 1: Geographical and geological settings of the studied outcrop. (**A)** Aerial image from Google Earth© of the area surrounding the studied outcrop, the southernmost cape of Mallorca: Cap Salines. (**B)** Map of Mallorca, with the main geological units and the names of the main Upper Miocene palaeogeographic areas. The green rectangle marks the location of the studied area shown in (A). (**C)** Sketch showing the general geological context of the Santanyí Limestone and the relationship with laterally adjacent units, the Bonanova Marls and the Tortonian–Messinian Mallorca Reef Complex. Modified after Arenas & Pomar (2010). The studied outcrop is part of the black facies with microbialites found at the top of the Miocene deposits in several places of the island (see text for details).

Fig. 2: Panoramic photographs of the western side of the studied outcrop, with its five different beds highlighted in green. Note the conspicuous darker colour of the biostrome of Bed 2. Green rectangles mark the location of close-up views in other figures. (**A)** Southern half of the outcrop. **(B)** Close-up of (A). **(C)** Northern half of the outcrop.

Fig. 3: Synthetic stratigraphic section of the studied outcrop, summarizing data from four sections measured at cm-scale at different points of the outcrop. Insert shows a sketch of the microbial biostrome, aim of this study, highlighting the different levels that compose it. Within the biostrome, orange marks the black-coloured grainstone deposits and purple the lighter-coloured microbialite deposits. M: mudstone; W: wackestone; P: packstone; G: grainstone.

Fig. 4: Macroscopic and microscopic features of Bed 1. **(A)** Outcrop aspect of Bed 1. **(B)** Detail of (A) showing poorly-preserved crossed-bedding**. (C)** Transmitted-light (TL) photomicrograph of oolitic–peloidal grainstone of Bed 1 with *Favreina*-like faecal pellets (green arrow). Orange arrows point to some mouldic pores, and yellow arrow to a vug-type pore. **(D)** TL photomicrograph of oolitic-peloidal grainstone of Bed 1 with abundant grapestones (pink arrows) and *Favreina*-like faecal pellets (green arrow). Yellow arrows point to some vug-type pores. **(E)** TL photomicrograph of peloidal wackestone–packstone of Bed 1. **(F)** Detail of the peloidal packstone microfacies with miliolid foraminifera (red arrows).

Fig. 5: (A) Outcrop aspect of the studied beds. Note the dark colour of Bed 2 and thinly-bedded to nodular aspect of Bed 3. Green rectangle marks the location of Fig. 7C. The metre stick (white vertical pole) is 90 cm long. **(B)** Outcrop detail showing the irregular, probably erosive, top of Bed 2 (yellow dashed line) and the variable thickness of Bed 3 (green arrows), adapting to the previous morphology of the underlying Bed 2. Note that the trough between domes of Bed 2 is filled with flat-pebble breccia of black and white intraclasts (see also Fig. 7A and B). Sledge-hammer (head *ca* 10 cm wide) at the middle-lower part for scale. Green rectangle marks the location of Fig. 7A. **(C)** Outcrop detail showing the changes in thickness of Bed 3 (green arrows), depending on the height of domes of Bed 2.

Fig. 6: Features of Beds 3 to 5. **(A)** Outcrop picture showing the changes in thickness of Bed 3 (green arrows), depending on the height of domes of Bed 2. **(B)** Outcrop aspect of the upper units of the outcrop (Beds 3 to 5). **(C)** Polarized-light (PL) photomicrograph of the recrystallized microfacies of Bed 3, with a microsparite layer in the lower part and pseudosparite in the middle and upper part, composed of a xenotopic mosaic of cloudy calcite crystals with irregular boundaries between them. **(D)** Transmitted-light (TL) photomicrograph of peloidal packstone of Bed 4, with scattered ostracods (green arrow) and subrounded lighter patches with less micrite (yellow arrows), probably representing bioturbation. **(E)** TL photomicrograph of peloidal packstone of Bed 5 with abundant *Favreina*-like faecal pellets (pink arrows) and subrounded grainstone patches, which may represent bioturbation (dashed yellow lines). (**F)** TL photomicrograph of peloidal–oolitic–bioclastic grainstone of Bed 4. Primary intergranular porosity, as well as secondary mouldic and vug-type pores, are partially filled by an isopachous rim of calcite cement (blue arrows). Isopachous calcite cement may be post-dated by a corrosion surface (red arrows), and/or by blocky calcite cement (green arrow). **(G)** TL photomicrograph of peloidal–oolitic grainstone of Bed 5. Primary intergranular porosity and secondary mouldic porosity are partially filled by an isopachous rim of calcite cement (blue arrows). Isopachous calcite cement may be postdated by a corrosion surface (red arrow), which is postdated by precipitation of opaque minerals both in primary and secondary pores (orange arrows). Locally, blocky calcite cement may occlude porosity (green arrow).

Fig. 7: Macroscopic features of the microbialite biostrome of Bed 2. **(A)** Outcrop detail of one of the domes of Bed 2 (with internal subdivision, 2a to 2d) and the base of Bed 3. Note the flat-pebble breccia of black and white intraclasts in the troughs between domes, at the left of the image. Green rectangles mark location of (G) and (H). **(B)** Detail of a trough between two domes of Bed 2, filled with flat-pebble breccia of black and white intraclasts. Yellow dashed line highlights the irregular, probably erosive, contact with overlying Bed 3. Tip of pen (green ellipse at the lower left) for scale, *ca* 2 cm long. **(C)** Outcrop aspect of Beds 1 to 3, with internal subdivision of Bed 2 (2a to 2d, note the contrasting colours). Green rectangle marks location of (E). Coin (centre of green rectangle) is 2.3 cm in diameter. **(D)** Outcrop detail of Bed 2. Note the different colours of its subdivisions, and the contrasting black colour and branching columnar structure of 2c (with columns lighter in colour than intercolumn spaces). **(E)** Outcrop detail of Bed 2. The internal structure of level 2c comprises: a thinner lower part formed by white dendritic tufts (Dendr.) and darker grainy deposits (Gr.), and a thicker upper columnar part (Col.) with lighter columns and darker intercolumn spaces. Coin is 2.3 cm in diameter. **(F)** Outcrop detail of level 2c in Bed 2 with its dendritic lower part (Dendr.) and the columnar upper part (Col.). Note the interruption level at the middle part of the columnar structure (yellow arrow at the left). Corner of field notebook, *ca* 6 x 6 cm, for scale at the lower left. **(G)** Detail of (A) showing the contact between the dendritic part (Dendr.) and the columnar part (Col.) of level 2c. Coin is 2.3 cm in diameter. **(H)** Detail of (A) showing the columnar structure of level 2c. Note the irregular contact between columns (lighter) and intercolumn spaces (darker). Coin is 2.3 cm in diameter.

Fig. 8: Transmitted-light (TL) photomicrographs of the microbialite level 2b of the Bed 2 biostrome. **(A)** Typical aspect of the strongly bioturbated microfacies of level 2b. Note the only rare remains of the original laminated microstructure (yellow arrows), strongly disrupted by the irregular bioturbation cavities and galleries, commonly lighter in colour. **(B)** Detail of left part in (A) with remains of the original finely laminated microstructure (yellow arrows). Note that bioturbated areas are filled by small peloids, clotted-peloidal micritic matrix and sparite cement. **(C)** Bioturbated microfacies of level 2b where the original laminated microstructure is well-preserved, including shrubby structures filled with calcite cement (green arrow). **(D)** Detail of the filamentous palisades of level 2b, with erect and branching tufts of micritic or pseudosparitic filaments. **(E)** Detail of the galleries and cavities (with their irregular borders highlighted by the yellow dotted line) that disrupt the original microbialite microstructures of level 2b.

Fig. 9: Thin lower part of level 2c of the Bed 2 biostrome. **(A)** Polished hand specimen of the thin lower part of level 2c, with its characteristic white dendritic structures, branching and widening upward, separated by black grainy deposits. **(B)** Transmitted-light (TL) photomicrograph of the black grainy deposits, with oolitic–peloidal grainstone texture. Note the abundant opaque Mn Ox/Hx that produce the black colour in outcrop. **(C)** TL photomicrograph of the branching tufts that form the white dendritic structures, separated by black oolitic–peloidal grainstone. Green rectangle marks location of (E). **(D)** Detail of thin branching tufts that form the white vertical dendritic structures. **(E)** Detail of (C), showing the recrystallized and faintly laminated clotted-peloidal micritic microfabric of the branching tufts, which are separated by darker grainstone, due to the abundance of opaque Mn Ox/Hx, much rarer within the tufts.

Fig. 10: Outcrop details of the thick upper part of level 2c of the Bed 2 biostrome. **(A)** Gradual lateral transition between branching columnar structure (Col.) left, and laminated structure (Lam.) right. In the columnar structure, note subvertical but irregular boundaries between columns (lighter) and intercolumn spaces (darker), and some light-coloured bridges joining adjacent columns (some marked with yellow arrows). **(B)** Weathered and exposed top surface of the columnar structure, showing the irregular distribution of columns (lighter) and intercolumn space (darker). Pen, 14 cm long, for scale at the top left. **(C)** Polished hand specimen showing gradual vertical transition between laminated structure (Lam.) below and columnar structure (Col.) above. Note the abundant light-coloured bridges joining adjacent columns (some marked with yellow arrows). **(D)** Uppermost part of a convex laminated structure with two rounded concave chamber-like structures disrupting lamination, similar to *Gastrochaenolites* borings. Green rectangle marks location of (F). Coin is 2.3 cm in diameter. **(E)** Weathered and exposed top surface (i.e. plan view) of a transitional area between laminated and columnar structure, showing intercolumn spaces filled by dark grey grainy sediment with irregular to subpolygonal distribution and rounded edges, reminiscent of *Thalassinoides* traces. Note that this structure penetrates downward several centimetres and that its diameter remains relatively constant, both along the bedding plane (green arrows) and in sections perpendicular or oblique to the stratification (red arrows). **(F)** Detail of the *Gastrochaenolites*-like borings shown in (D). The left one includes a gastropod cast (yellow arrow).

Fig. 11: Transmitted-light (TL) photomicrographs of the laminated structure of level 2c of the Bed 2 biostrome. **(A)** Alternation of thinner darker laminae with thicker lighter ones, the latter often showing filamentous and shrubby structures perpendicular to lamination (green arrows). Pink dotted line highlights an irregular patch of dark oolitic–peloidal grainstone disrupting lamination. Green rectangle marks location of (B). **(B)** Close-up of (A) with details of a filamentous shrubby structure (below), a dense to clotted peloidal dark lamina (middle) and an open irregular clotted-peloidal fabric (above). **(C)** Transitional area between laminated structure (left) and columnar structure (right). Pink dotted lines highlight the boundary of dark grainy intercolumn space and of some patches within the laminated structure, filled with dark grainy sediment and/or calcite cement. Yellow arrows point to very fine and microdomed lamination. Green arrows point to filamentous and shrubby structures perpendicular to lamination. Green rectangle marks the location of (D). **(D)** Close-up of (C) with a detail of the irregular boundary of dark grainy intercolumn space (right). Note that this boundary seems to cut microbialite lamination (left).

Fig. 12: Transmitted-light (TL) photomicrographs of the columnar structure of level 2c of the microbialite biostrome (Bed 2). **(A)** Columns are internally formed of a lighter-coloured, highly open clotted-peloidal micrite microstructure with faint traces of convex lamination (red arrows) and poorly-preserved fan-like or tufted filamentous microstructure (green arrows). Intercolumn spaces are filled by grainy sediment, darker in colour due to abundant opaque Mn Ox/Hx, with common concave lamination (yellow arrows). Note the irregular contact between columns and intercolumn spaces, and some irregular cavities within the columns filled by dark grainy sediment (one of them highlighted in pink dotted line). Green rectangles mark location of (B) and of Fig. 13A and B. **(B)** Close-up of (A) showing microstructure details of both columns and intercolumns. Green arrows point to poorly-preserved fan-like or tufted filamentous structures within the columns. Yellow dotted lines highlight light-coloured clotted-peloidal bridges joining adjacent columns.

Fig. 13: Detailed transmitted-light (TL) photomicrographs of the columnar structure of level 2c of the microbialite biostrome (Bed 2). **(A)** Close-up of Fig. 12A showing microstructure details of both columns and intercolumns. Within the light-coloured columns, green arrows point to poorly-preserved fan-like or tufted filamentous structures, and red dotted line highlights faint convex lamination. Within the dark-coloured intercolumns, yellow dotted lines highlight clotted-peloidal

bridges joining adjacent columns. **(B)** Close-up of Fig. 12A showing the grainy and dark intercolumn between two columns. Note the irregularity of the contact between them and the local presence of a micritic wall (blue arrows).

Fig. 14: Microscopic features of level 2d of the Bed 2 biostrome. **(A)** Transmitted-light (TL) photomicrograph of a calcite pseudomorph after a euhedral mineral (probably an evaporite), within a recrystallized pseudosparitic matrix. **(B)** TL photomicrograph of finely-laminated microstructure with unfilled pseudomorphs after subhedral minerals, which grew displacing lamination.

Fig. 15: Some diagenetic aspects of the microbialite biostrome (Bed 2) that help to understand its black colour in outcrop. **(A)** Transmitted-light (TL) photomicrograph of the boundary (yellow arrow) between a microbialite column (left), and the oolitic–peloidal grainstone of the intercolumn space (right). Ooids and peloids may be totally or partially replaced by opaque Mn Ox/Hx (green arrows). Manganese Ox/Hx can be also observed along the limit between both microfacies (yellow arrow) and also, locally, within microbialite (red arrow). Precipitation of Mn Ox/Hx is postdated by non-ferroan blocky calcite cement, which may completely fill porosity. **(B)** TL photomicrograph of the irregular boundary between a microbialite column (right), and the oolitic–peloidal grainstone of the intercolumn space (left). Mn Ox/Hx replace partially or totally ooids and peloids (green arrow) and are scarcely observed within the microbialite (red arrows). Blocky non-ferroan calcite cement occludes porosity. **(C)** and **(D)** Scanning electron microscopy (SEM) images of the oolitic and peloidal facies containing abundant Mn Ox/Hx, which are filling primary porosity and replacing calcite (Cc) grains and/or cements (orange arrows). Note the mouldic pores (blue arrows), and the external rounded shape of a grain surrounded by Mn Ox/Hx (yellow arrow). **(E)** TL photomicrograph of a microbialite column. Mn Ox/Hx replace partially the clotted-peloidal micrite and surround the border of a vug-type pore. Porosity is occluded by precipitation of non-ferroan blocky calcite cement. **(F)** and **(G)** TL and cathodoluminescence (CL) photomicrographs, respectively, of a secondary pore (mouldic) of microbialite, which is filled by non-ferroan and non-luminescent (G) blocky calcite cement. Note the thin euhedral rim of calcite (blue arrows) displaying brownish colour, under TL (F), and bright orange-reddish colour, under CL (G). **(H)** and **(I):** TL and CL photomicrographs, respectively, of a peloidal packstone–grainstone. Peloids are partially or totally replaced by Mn Ox/Hx and display patchy orange

luminescence (when partially replaced) or are non-luminescent when totally replaced. Porosity is occluded by non-ferroan and non-luminescent blocky calcite cement. The limit between the grains and calcite cement is commonly marked, under CL (I), by a thin bright orange luminescent rim. **(J)** and **(K)** TL and CL photomicrographs, respectively, of a secondary pore (mouldic) of microbialite, which is filled by non-ferroan and non-luminescent blocky calcite cement. Clotted-peloidal micrite displays dull orange-brownish luminescence.

Fig. 16: Two contrasting morphogenetic models of columnar microbialites. Sketches are not to scale, although columns are typically a few centimetres wide. **(A)** Simplified sketch of archetypical Proterozoic columnar stromatolites, formed exclusively by microbial accretion and grainy sedimentation between the columns. Inspired in examples figured by Walter (1972), Bertrand-Sarfati (1972) and Grey & Awramik (2020). **(B)** New morphogenetic model presented here for microbialites (mainly Phanerozoic, but probably also Upper Proterozoic) whose columnar morphology is influenced by bioturbation during or very soon after microbial accretion, as well as grainy sedimentation between the columns. Inspired in the examples described here and those figured by Cao (1988). Note the highly irregular boundary between columns and intercolumn spaces, which includes only locally a micritic wall (thicker and darker line), in contrast to (A).

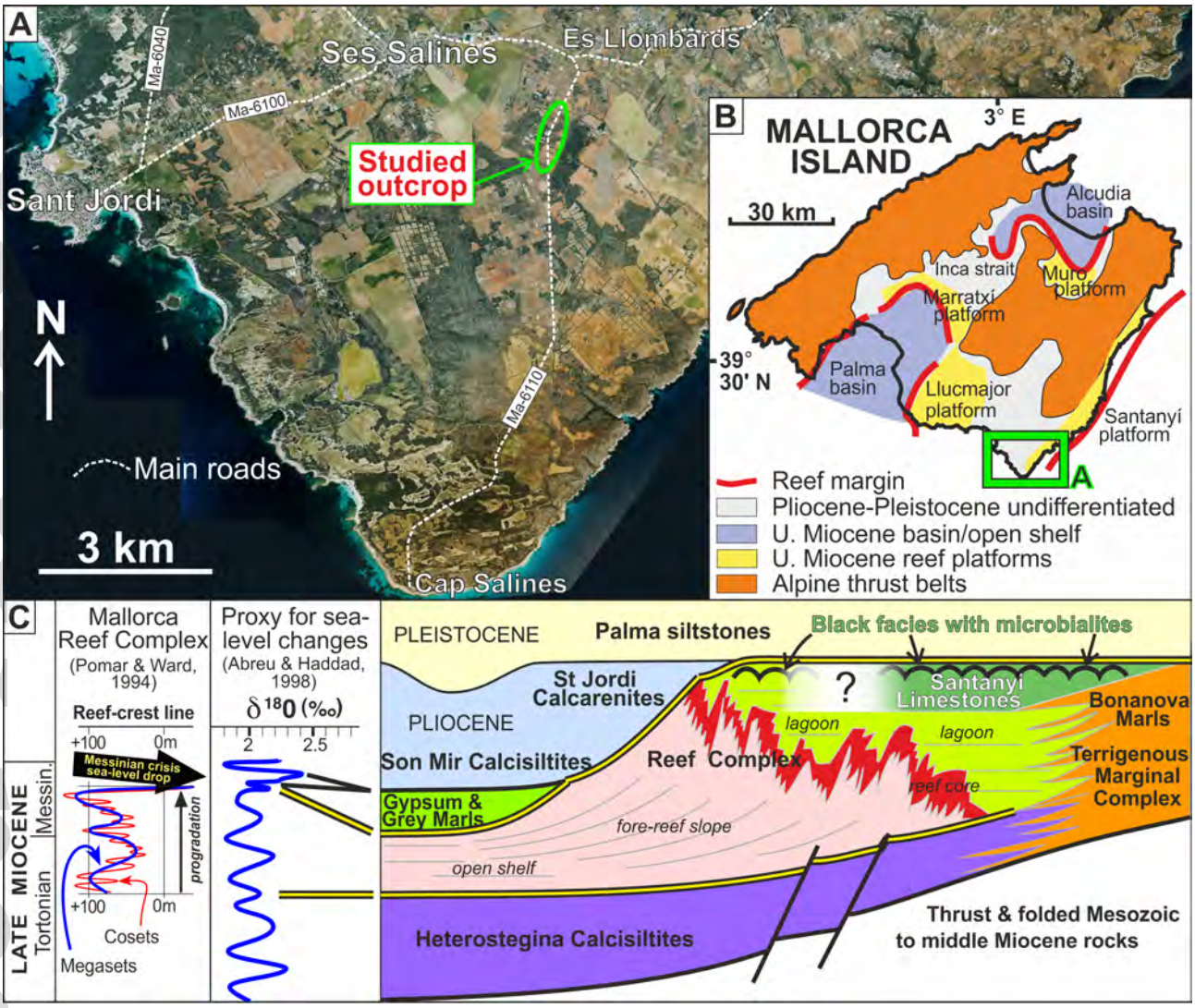

sed_12850_f1.tif

sed_12850_f2.tif

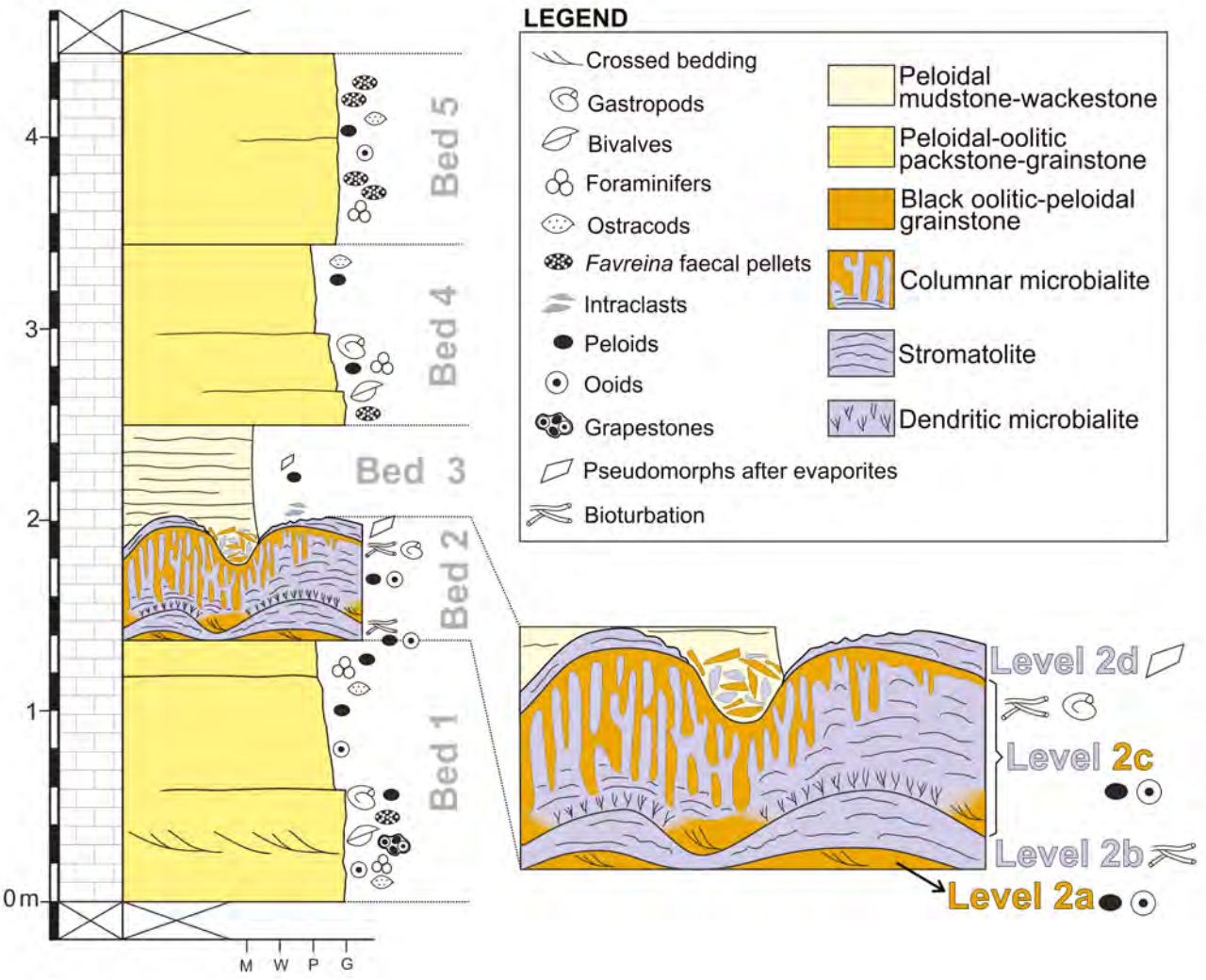

sed_12850_f3.tif

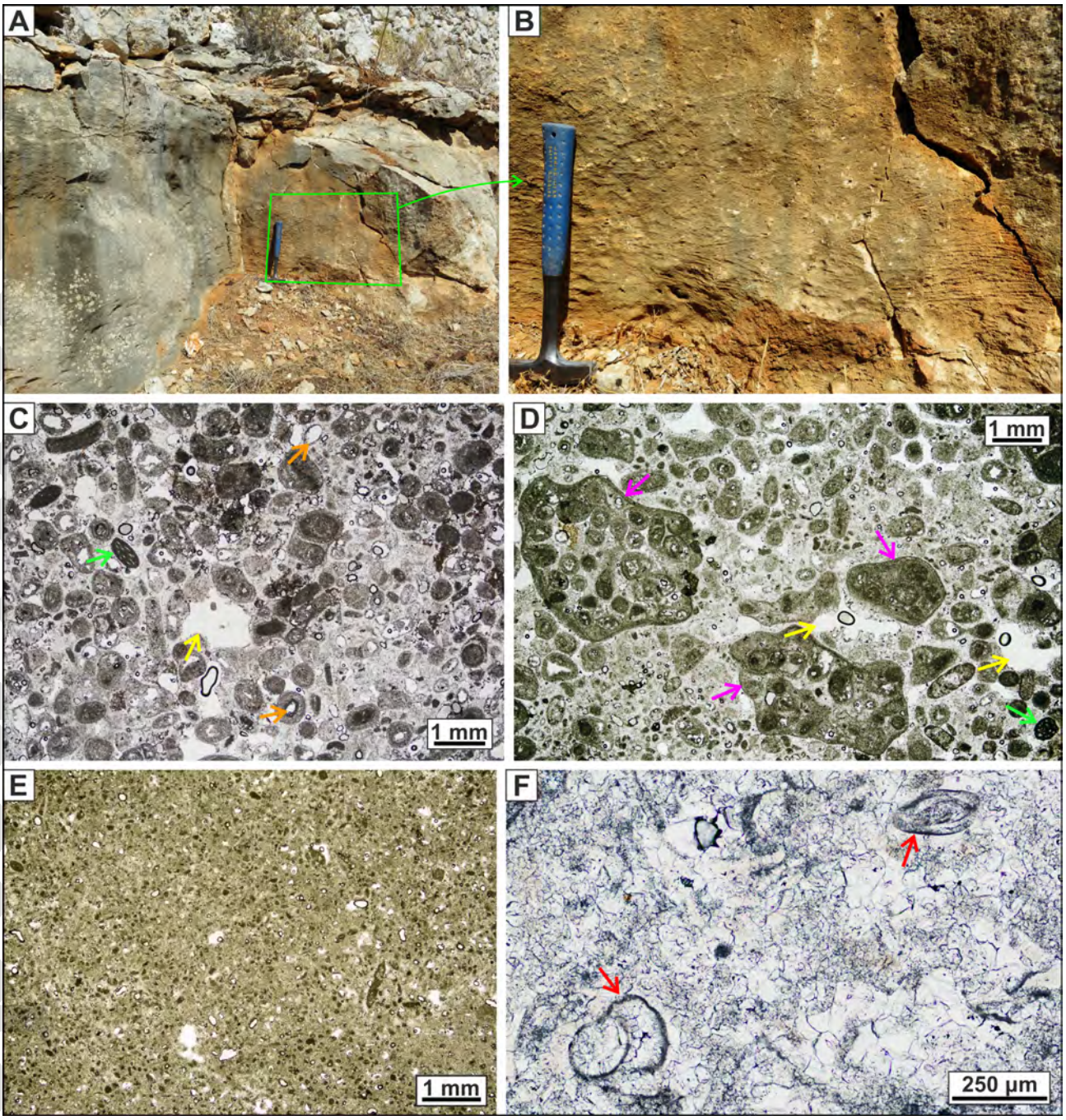

sed_12850_f4.tif

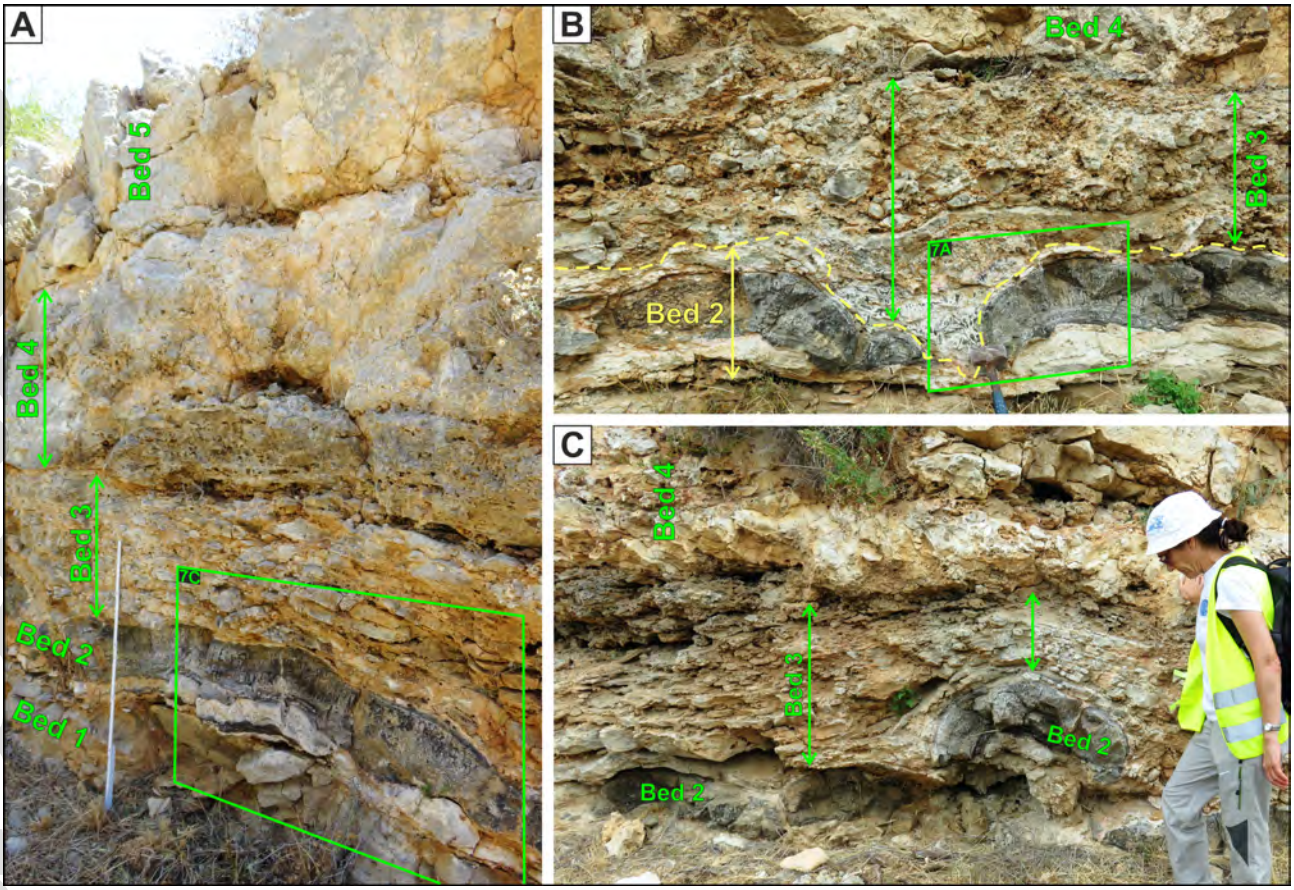

sed_12850_f5.tif

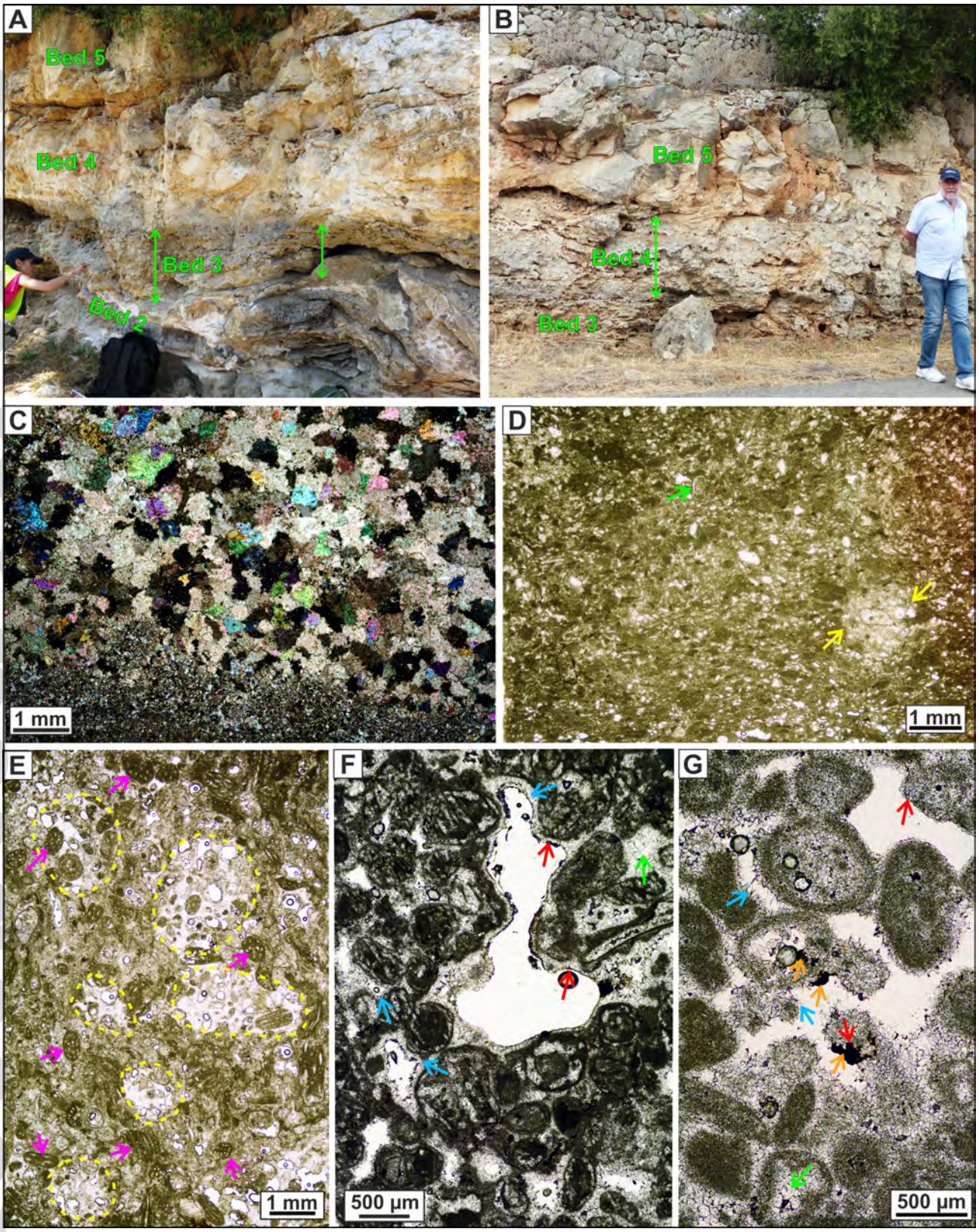

sed_12850_f6.tif

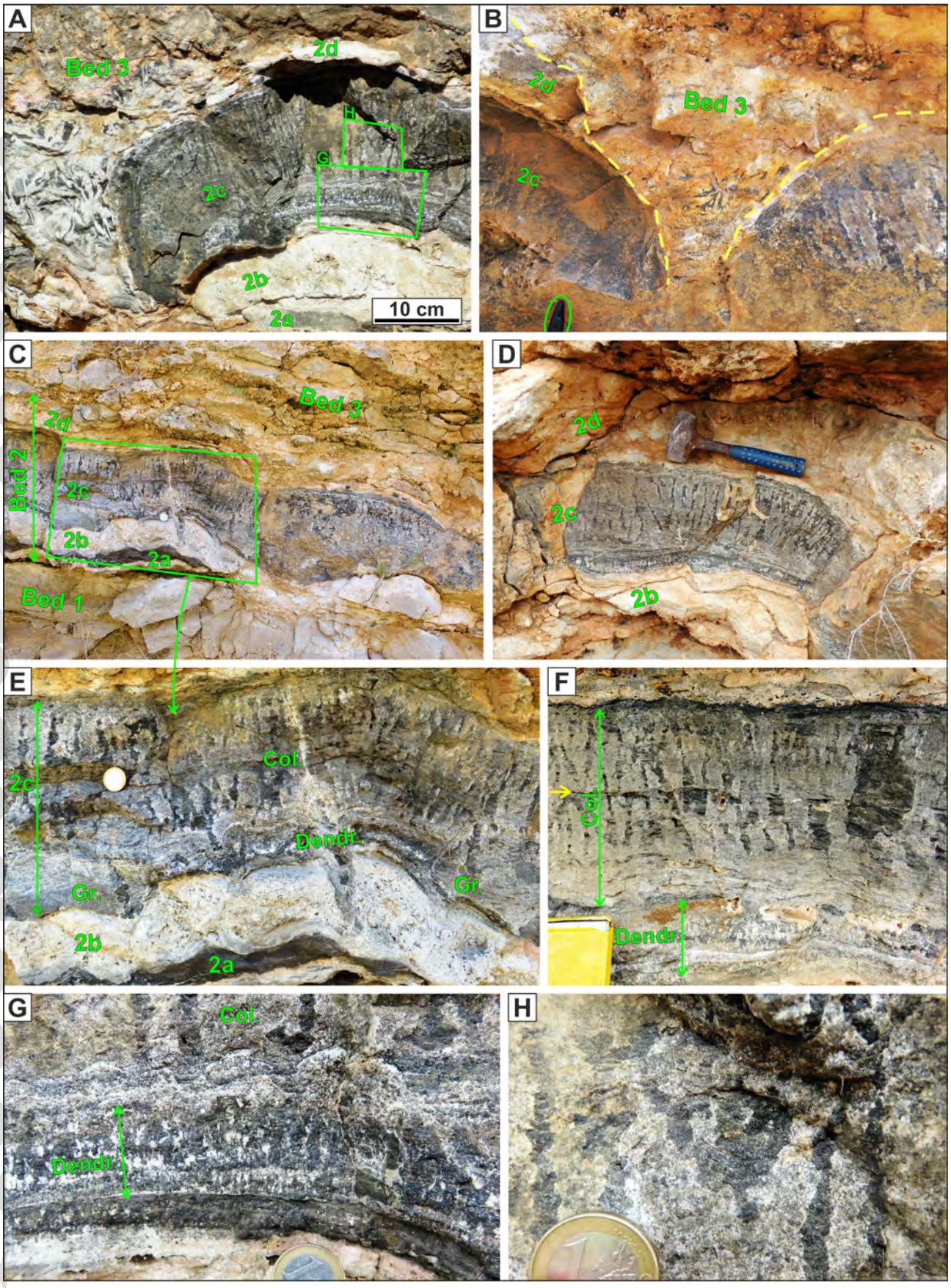

sed_12850_f7.tif

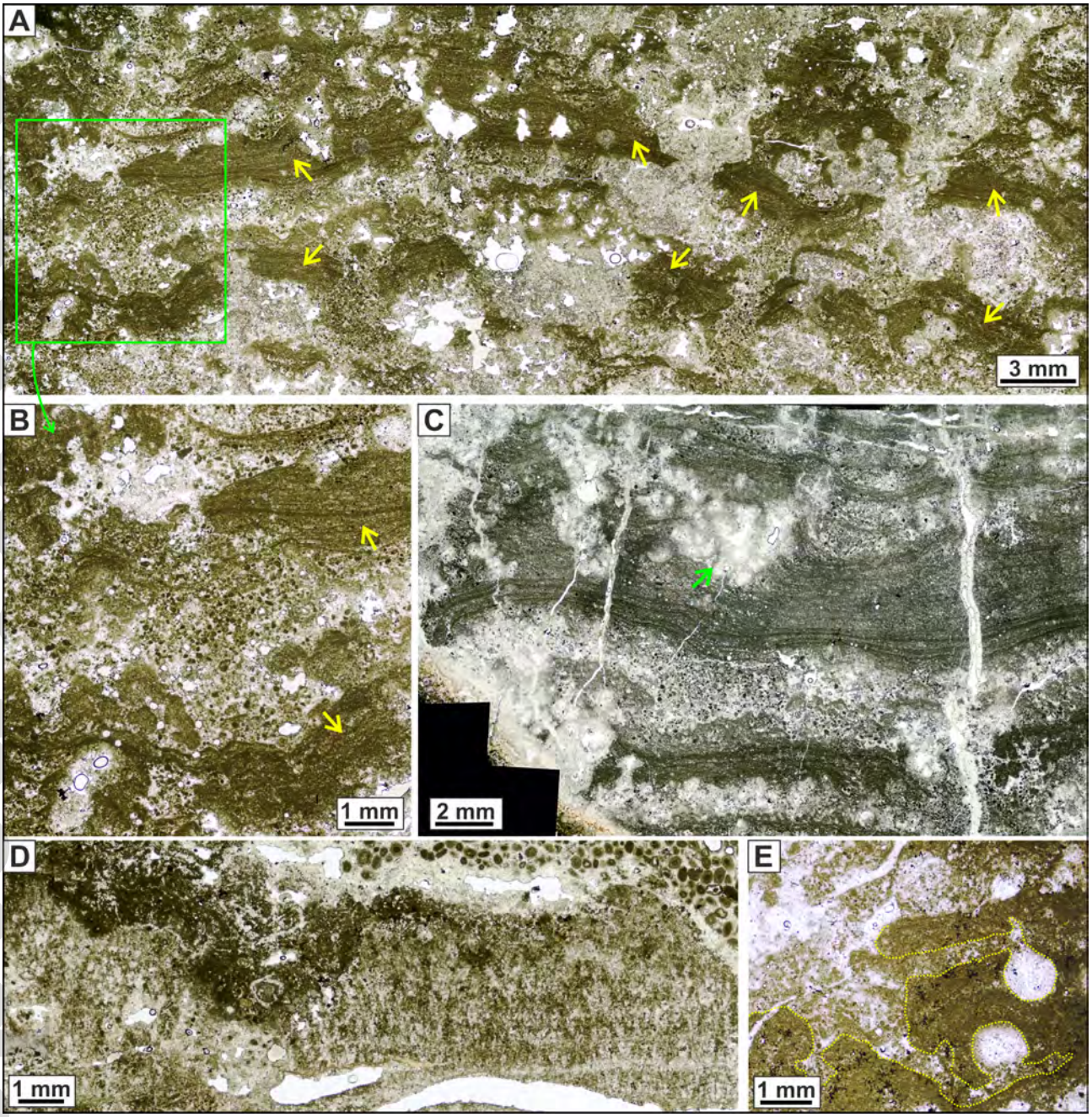

sed_12850_f8.tif

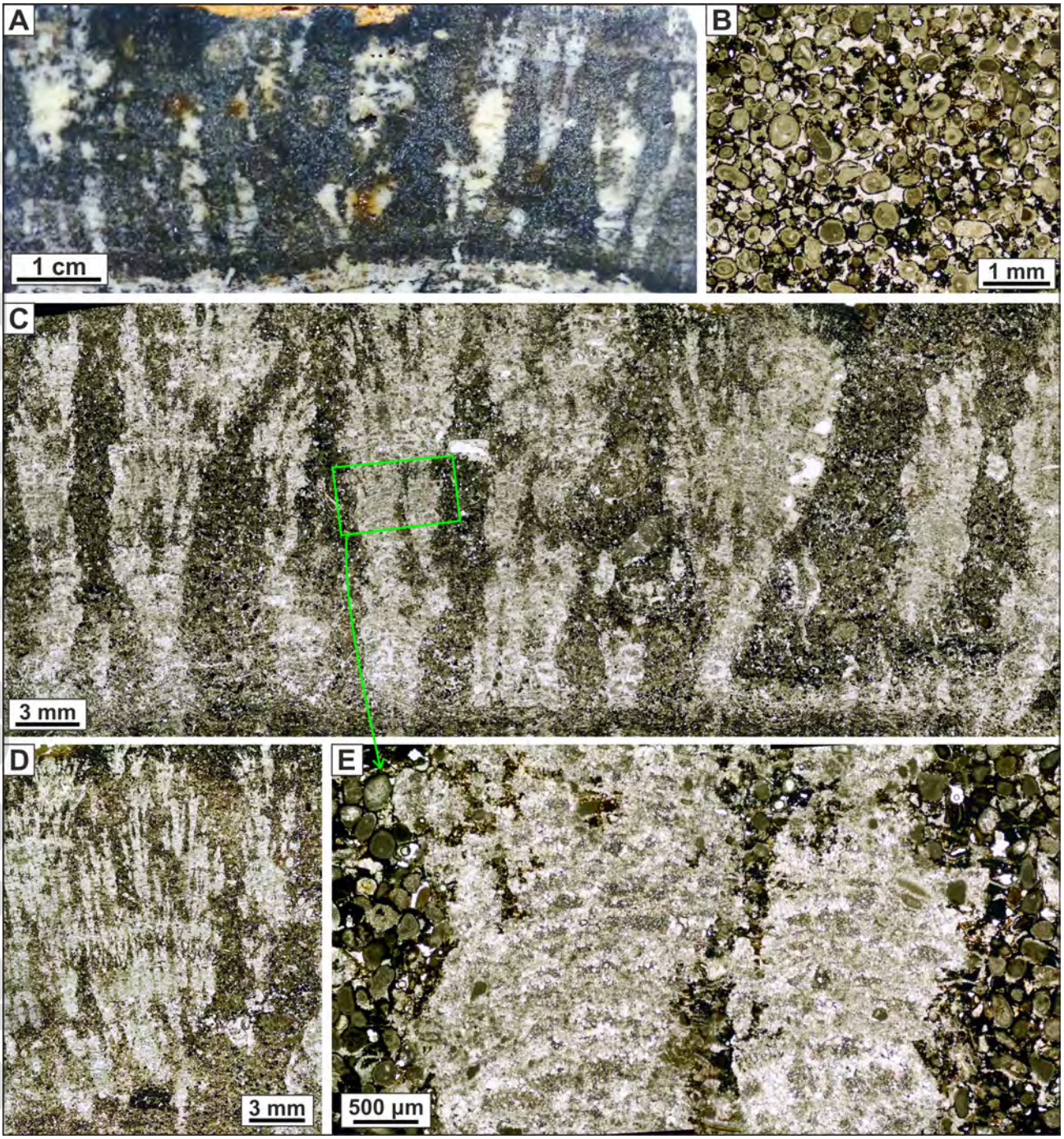

sed_12850_f9.tif

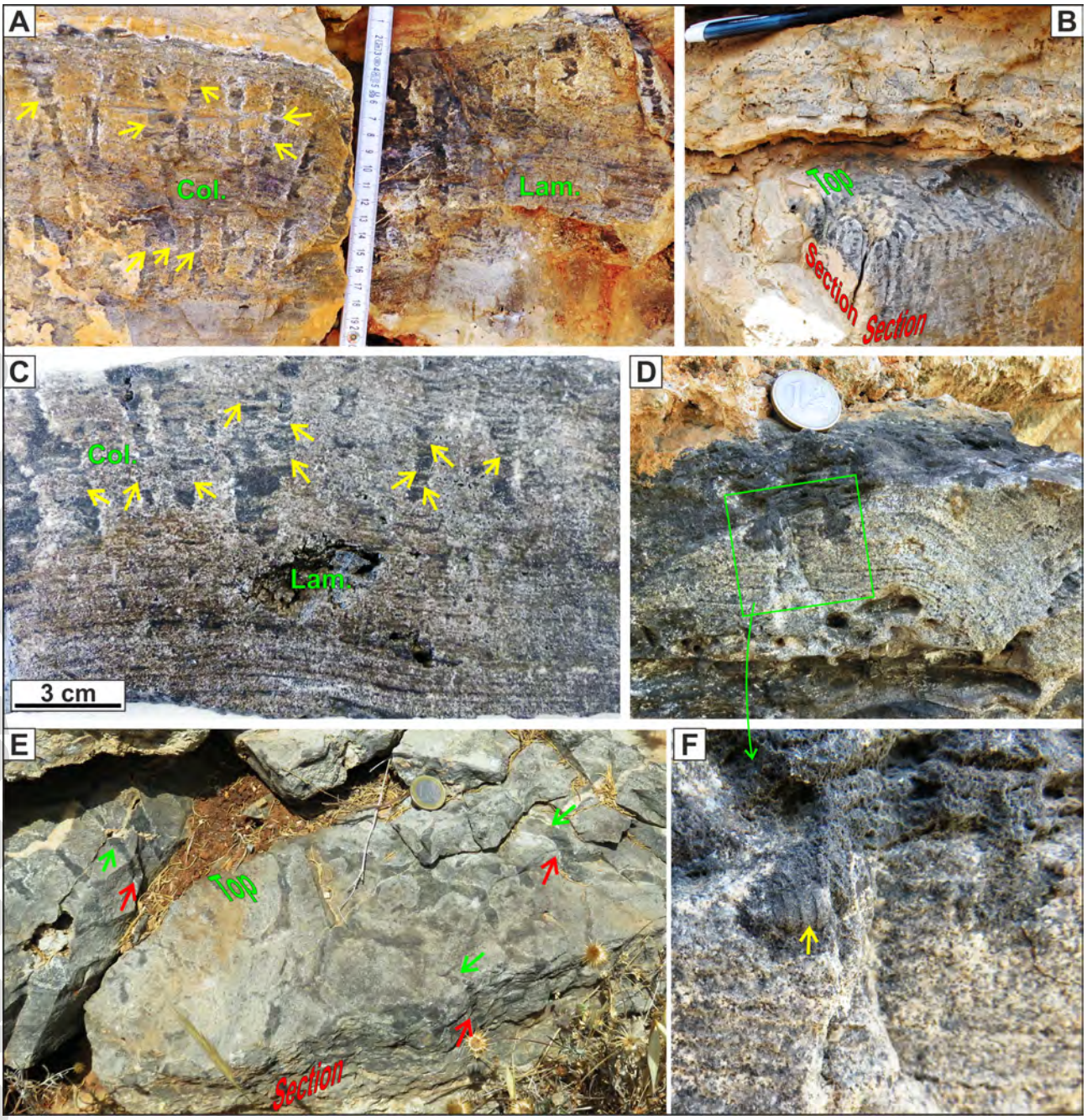

sed_12850_f10.tif

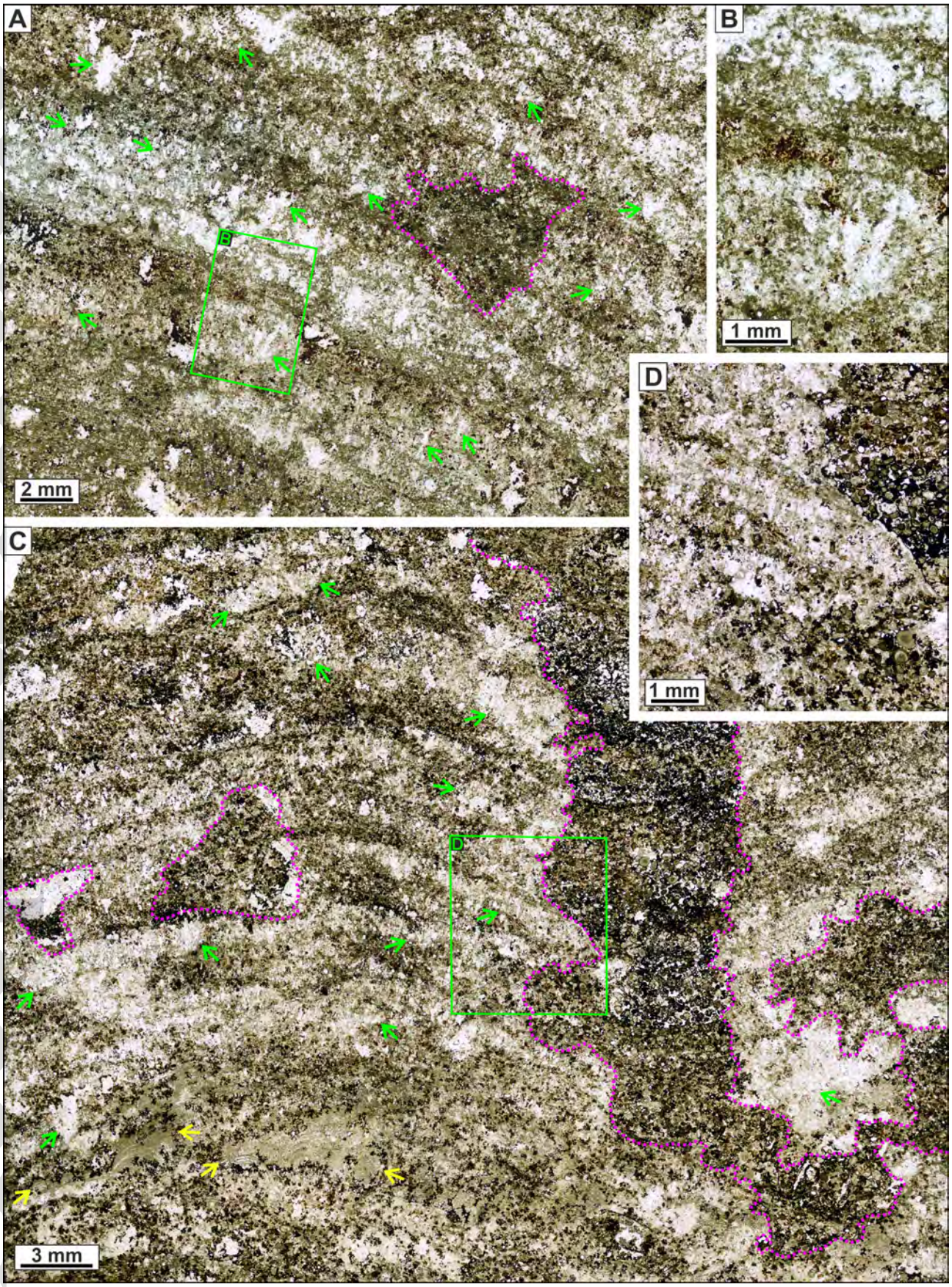

sed_12850_f11.tif

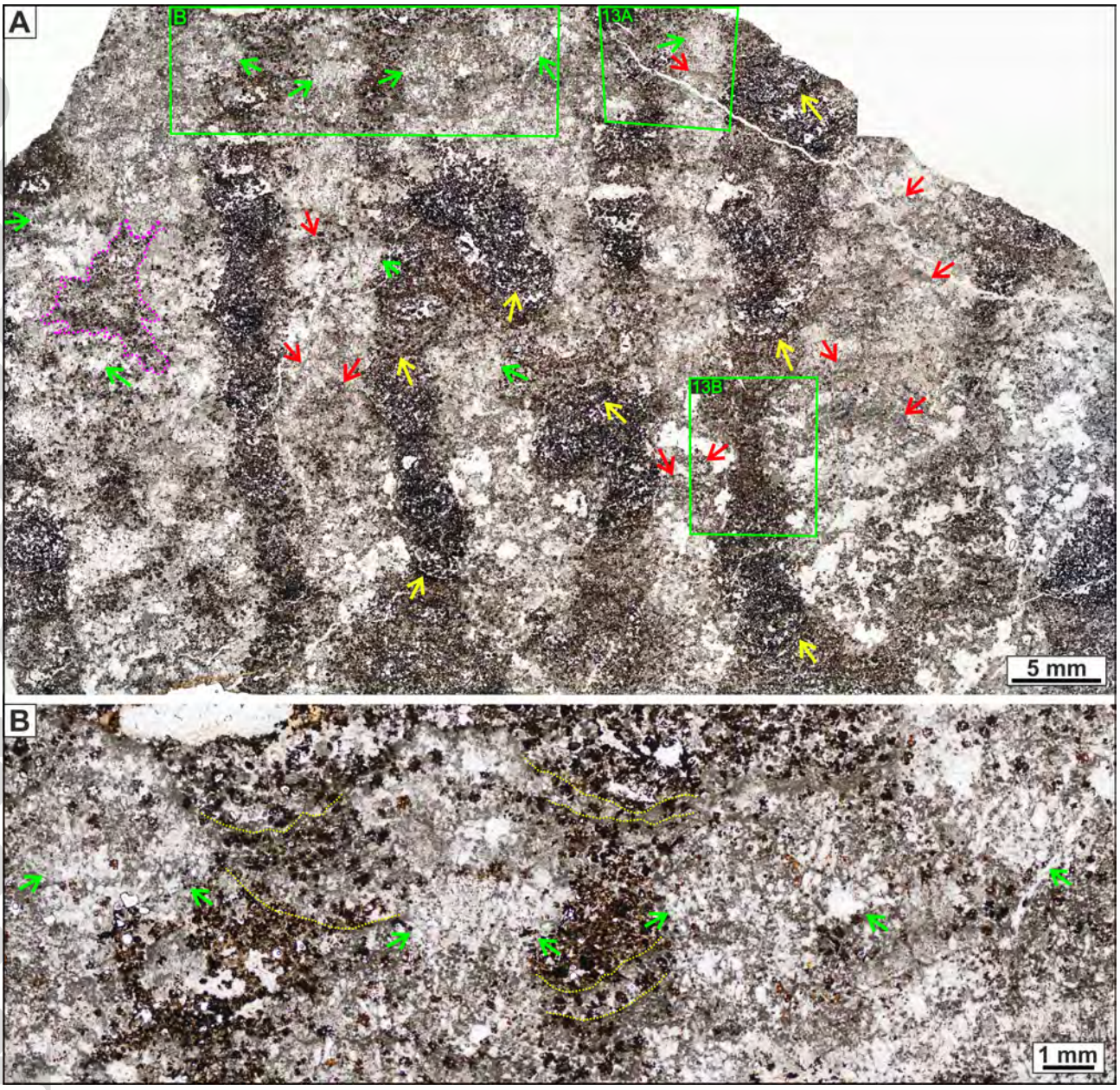

sed_12850_f12.tif

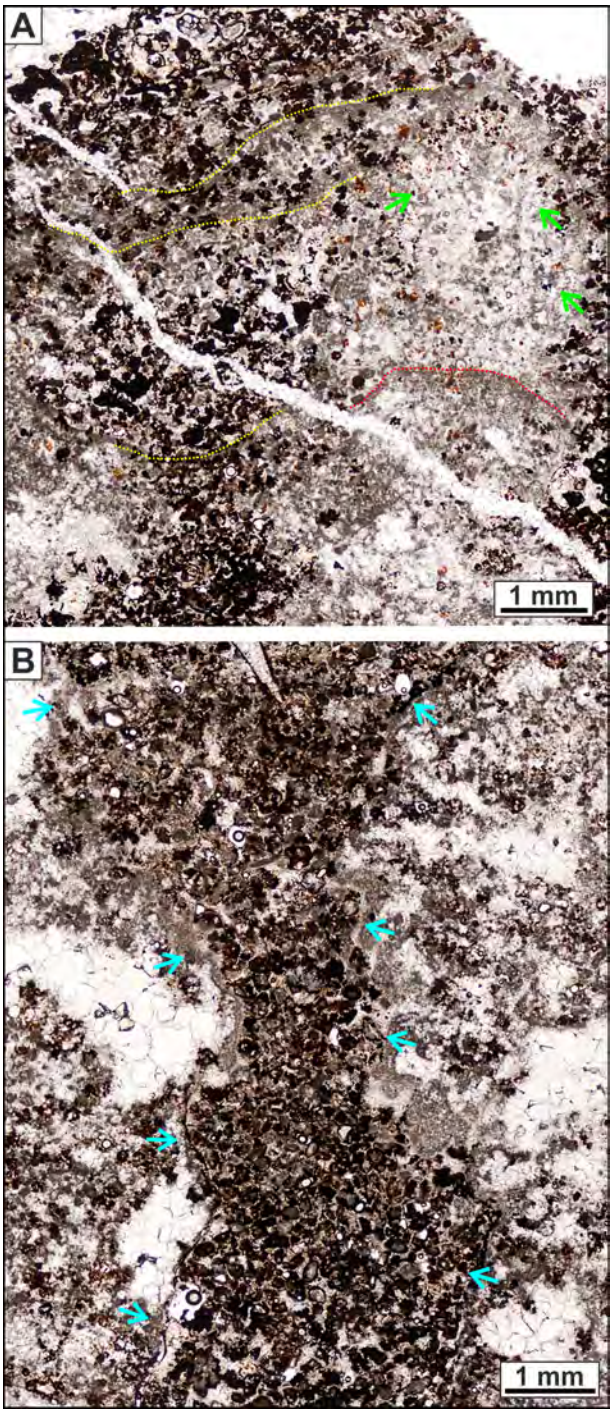

sed_12850_f13.tif

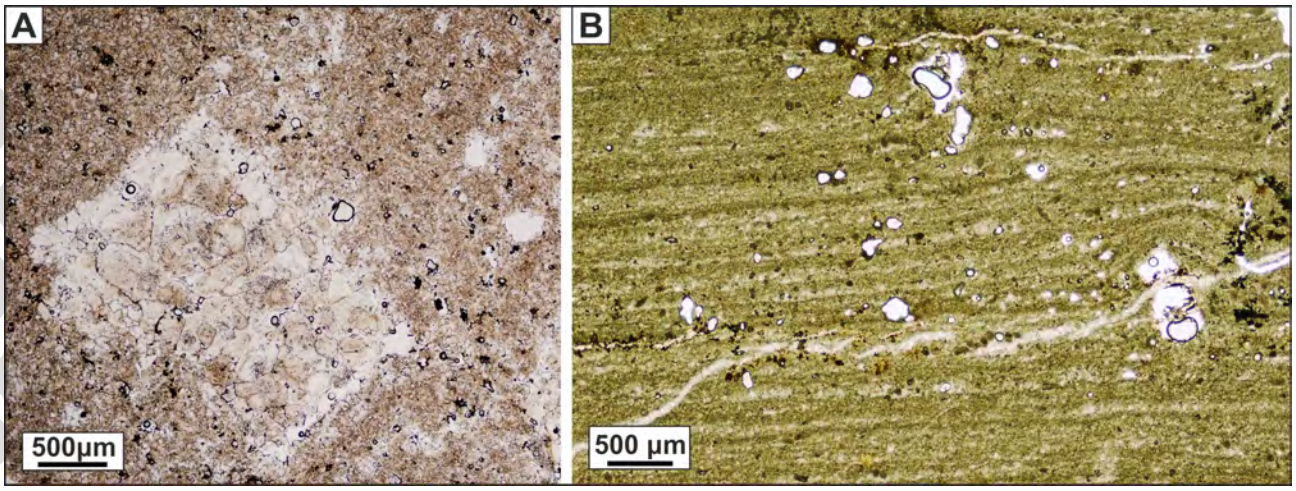

sed_12850_f14.tif

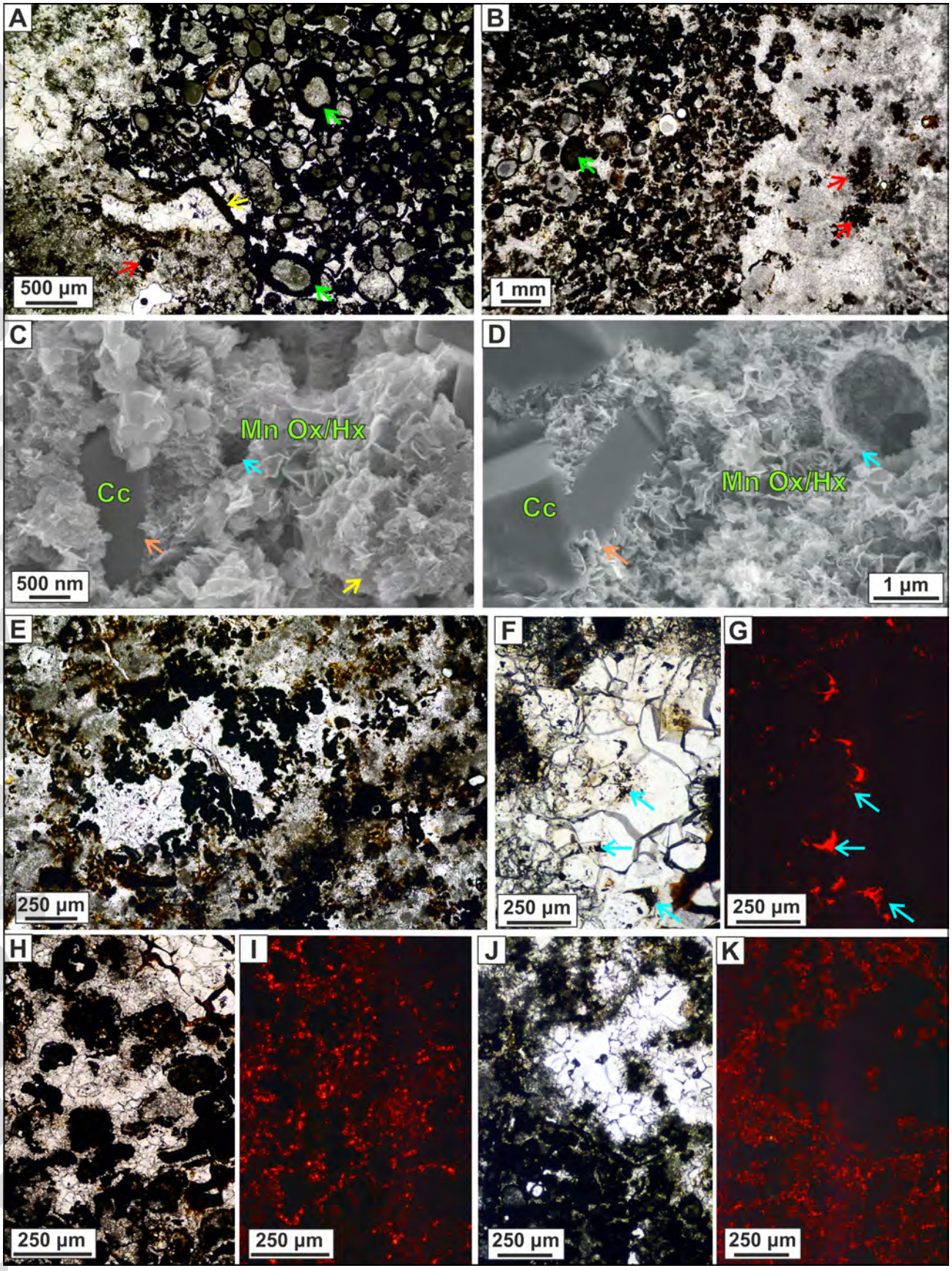

sed_12850_f15.tif

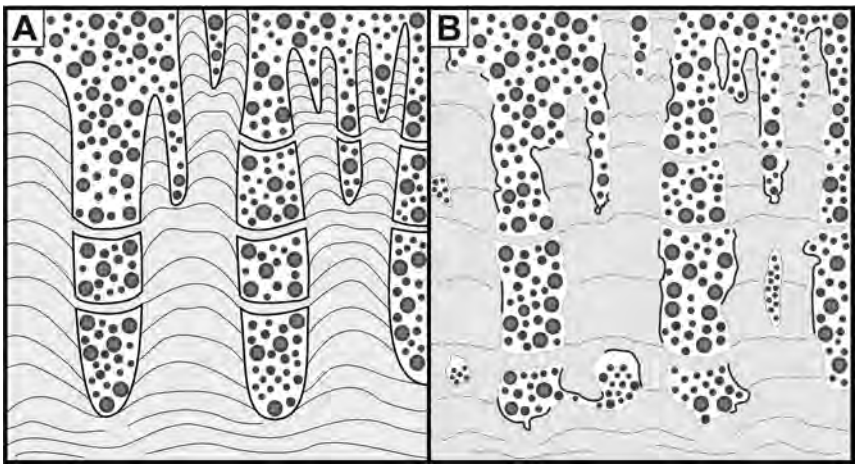

sed_12850_f16.tif